

# An original potentiating mechanism revealed by the cryoEM structures of the human $\alpha 7$ nicotinic receptor in complex with nanobodies

PREVOST Marie S.<sup>1#\*</sup>, BARILONE Nathalie<sup>1#</sup>, DEJEAN DE LA BATIE Gabrielle<sup>1</sup>, PONS Stéphanie<sup>2</sup>, AYME Gabriel<sup>3</sup>, ENGLAND Patrick<sup>4</sup>, GIELEN Marc<sup>1,5</sup>, BONTEMS François<sup>6,7</sup>, PEHAU-ARNAUDET Gérard<sup>8</sup>, MASKOS Uwe<sup>2</sup>, LAFAYE Pierre<sup>3</sup>, CORRINGER Pierre-Jean<sup>1\*</sup>

1 Institut Pasteur, Université Paris Cité, CNRS UMR 3571, Channel-Receptors Unit, Paris, France

2 Institut Pasteur, Université Paris Cité, CNRS UMR 3571, Integrative neurobiology of cholinergic systems Unit, Paris, France

3 Institut Pasteur, Université Paris Cité, CNRS UMR 3528, Antibody Engineering platform, Paris, France

4 Institut Pasteur, Université Paris Cité, CNRS UMR 3528, Molecular Biophysics platform, Paris, France

5 Sorbonne Université, Paris, France

6 Institut Pasteur, Université Paris Cité, CNRS UMR 3569, Structural Virology unit, Paris, France

7 Institut de chimie des substances naturelles, Centre national de la recherche scientifique, Université Paris Saclay, Gif-sur-Yvette, France

8 Institut Pasteur, Université Paris Cité, Ultrastructural Bioimaging Core facility, Paris, France

# equal contribution

\* Corresponding authors

Email:

[marie.prevost@pasteur.fr](mailto:marie.prevost@pasteur.fr)

[pierre-jean.corringer@pasteur.fr](mailto:pierre-jean.corringer@pasteur.fr)

## Abstract

The human  $\alpha 7$  nicotinic receptor is a pentameric channel mediating cellular and neuronal communication. It has attracted considerable interest to design ligands for the treatment of neurological and psychiatric disorders. To develop a novel class of  $\alpha 7$  ligands, we recently generated two nanobodies named E3 and C4 acting as positive and silent allosteric modulators respectively. Here, we solved the cryo-EM structures of the nanobody-receptor complexes. E3 and C4 bind to a common epitope involving two subunits at the apex of the receptor. They form by themselves a symmetric pentameric assembly that extends the extracellular domain. Unlike C4, the binding of E3 drives an active or desensitized conformation in the absence of orthosteric agonist, and mutational analysis shows a key contribution of a N-linked sugar moiety in mediating E3 potentiation. The nanobody E3, by remotely controlling the global allosteric conformation of the receptor, implements an original mechanism of regulation which opens new avenues for drug design.

# Introduction

Nicotinic acetylcholine receptors (nAChRs) mediate cellular communication in neuronal and non-neuronal cells. In humans, sixteen genes encode for nAChRs subunits that can assemble into homo- or hetero-pentamers, generating a wide diversity of combinations each displaying an unique expression pattern and physiological function<sup>1</sup>. Among nAChRs, the homopentameric  $\alpha 7$  has attracted considerable interest with the aim of developing enhancers for the treatment of neurological and psychiatric disorders associated with cognitive decline such as Alzheimer's disease, schizophrenia, autism or bipolar troubles<sup>2</sup>. The  $\alpha 7$ -nAChR is also an essential component of the cholinergic anti-inflammatory pathway<sup>3</sup>.

nAChRs are pentameric ligand-gated ion channels (pLGIC). Acetylcholine (ACh) binding to the orthosteric site within their extracellular domain (ECD) promotes the fast transition from a resting closed-channel state to an active open-channel state selective for cations. This is followed by a slower transition to a desensitized closed-channel state.  $\alpha 7$ -nAChR specific agonists and partial agonists have been developed, some of which display pro-cognitive effects in pre-clinical trials<sup>4</sup>. Positive allosteric modulators (PAMs) binding in the transmembrane domain (TMD) also showed beneficial effects, as exemplified by the Type II PAM PNU-120596 (PNU) which potentiates the ACh-elicited currents and strongly impairs desensitization<sup>5</sup>.

Several human  $\alpha 7$ -nAChR high-resolution structures have recently been solved by cryo-electron microscopy (cryoEM), in detergent micelles or in protein/lipid nanodiscs<sup>6,7</sup>.  $\alpha 7$ -nAChR harbours a  $\beta$ -folded ECD carrying the orthosteric site at the interface between subunits, coupled to a TMD with 4  $\alpha$ -helices per subunit (termed M1 to M4) that form the ion channel, and an intracellular domain (ICD), which contains two helices (MA and MX) flanking a highly variable region which is truncated in the constructs used for solving cryo-EM structures. Closed-channel structures in Apo and antagonist (bungarotoxin (Bgt))-bound conditions have been annotated as resting conformations, while those in complex with agonists (epibatidine or EVP-6124 abbreviated as EVP) have been annotated as desensitized conformations. Structures in complex with both agonist and PNU show an apparently open (Epi) or semi-open (EVP) pore, consistent with an active and partially-active state, respectively<sup>8</sup>.

The comparison of the resting and open or semi-open conformations shows that agonist binding promotes a contraction of the orthosteric site involving a large inward movement of the C-loop that caps the binding cavity. This is associated with a twist and tilt of each subunit  $\beta$ -sandwich. The tilt moves the upper part of the subunit ECD towards its neighbouring complementary subunit, while its lower part moves away from it. In consequence, the cys-loop at the bottom of the ECD undergoes an outward movement associated with TMD expansion, M2 tilt and channel opening. From this open-channel conformation, desensitization motions mainly concern the TMD that relaxes back towards an occluded, closed-channel conformation, associated with a subtle global expansion of the ECD.

In a previous study, we immunized alpacas with cells expressing an  $\alpha 7/5HT_3$  chimera to generate highly potent and  $\alpha 7$ -specific modulators<sup>9</sup>. Among the resulting camelid antibody fragments called nanobodies, the one called E3 acts as a Type I PAM. In two electrode voltage-clamp electrophysiology (TEVC), upon pre-application for 30-60 sec, E3 potentiates ACh-gated currents with a maximal effect around an EC<sub>10</sub> concentration of ACh of 30  $\mu$ M. E3 does not alter significantly the EC<sub>50</sub> of ACh, nor the apparent slow desensitization component of the ACh-elicited response. In contrast, the nanobody called C4 acts as a silent allosteric modulator (SAM), showing no effect on ACh-gated currents but inhibiting E3-elicited potentiation. Both nanobodies do not displace Bgt in binding experiments, pointing to an allosteric binding site away from the orthosteric site.

In this paper, we aim at understanding the mechanism by which the nanobodies mediate their allosteric effect by solving the cryoEM structures of the complexes they form with the  $\alpha 7$ -nAChR. Our data enables the high-resolution identification of the common binding epitope targeted by C4 and E3, with in both cases an association of five nanobodies binding at the top of the receptor pentamer. Mutational investigations hint at a key N-linked sugar moiety in mediating E3 potentiation.

## Results

### *1/ Production of the purified human $\alpha 7$ -nAChR reconstituted in nanodiscs*

To express the  $\alpha 7$ -nAChR in mammalian cells, we used a lentivirus-based strategy<sup>10</sup> (Figure S1). We designed two lentiviral constructs harbouring a gene coding for either the full-length  $\alpha 7$ -nAChR subunit fused to a Rho1D4 tag at its C-terminus ( $\alpha 7$ FLcryo) or for the same gene where the coding sequence of the ICD is replaced by a short linker based on a  $\alpha 4\beta 2$  construct used for crystallogenes<sup>11</sup> ( $\alpha 7\Delta$ ICDcryo) (Figure S2). We additionally produced a lentiviral construct harbouring the coding sequence of the chaperone NACHO<sup>12</sup>. Lentiviruses particles were used to infect T-REx cells grown in suspension. Expressed proteins were affinity purified in dodecyl-maltoside (DDM). As initial micrographs in detergent micelles showed protein aggregation, we further reconstituted the protein in MSP1E3D1 nanodiscs containing brain lipid extracts, resulting in well dispersed particles on cryoEM grids (Figure S1). Yields of production were improved around 2-fold in the  $\alpha 7\Delta$ ICDcryo construct as compared  $\alpha 7$ FLcryo. In parallel, we expressed and purified C4 and E3 nanobodies in a monomeric form as described previously<sup>9</sup> (Figure S1 and S3).

We first verified that both  $\alpha 7$ cryo constructs retain the modulation properties of C4 and E3 in TEVC (Figures S1). As for the wild-type  $\alpha 7$  nAChR, a pre-incubation of 1 $\mu$ M of E3 leads to the potentiation of ACh-gated currents with no apparent effect on desensitization. C4 pre-incubation has no significant effect by itself but inhibits E3-elicited potentiation (Figure S1). We also measured the binding affinity of both nanobodies for the nanodiscs-reconstituted  $\alpha 7\Delta$ ICDcryo using single cycle kinetics Surface Plasma Resonance assays. In both cases, Rmax values suggest a maximum of three nanobodies molecules bound per receptor molecule. Concentration-response curves show that C4 displays slower association and dissociation kinetics ( $k_{on} = 1.2 \pm 0.05 \cdot 10^6 \text{ M}^{-1} \cdot \text{s}^{-1}$ ,  $k_{off} = 0.024 \pm 0.02 \cdot 10^{-2} \text{ s}^{-1}$ ) than E3 ( $k_{on} = 11 \pm 0.02 \cdot 10^6 \text{ M}^{-1} \cdot \text{s}^{-1}$ ,  $k_{off} = 1.19 \pm 0.01 \cdot 10^{-2} \text{ s}^{-1}$ ). Data show high affinity for both C4 and E3 with Kd of  $0.2 \pm 0.3 \text{ nM}$  and  $1 \pm 0.01 \text{ nM}$  respectively (Figure S4). We also assayed E3 in the presence of nicotine, to investigate whether a possible increased affinity could account for its PAM action. However, the affinity of E3 was found identical in the absence and presence of nicotine (Figure S4).

### *2/ Cryo-EM structures of $\alpha 7$ in complex with C4 show preservation of nicotine-elicited reorganizations*

We first solved the cryo-EM structure of the  $\alpha 7\Delta$ ICDcryo in the presence of a 50-fold excess of C4 (1 $\mu$ M  $\alpha 7$  pentamer for 50 $\mu$ M C4, C4-Apo structure) (Figure 1 and S5, table S1). After 2D and 3D classifications, the final set of particles yielded a 5-fold symmetrical reconstruction, with five bound nanobodies per  $\alpha 7$  pentamer. For most of the ECD and nanobodies, the density map is of good quality and allows to confidently build the main and side chains of the protein with a nominal resolution of 2.3 Å. In contrast, the density of the TMD and associated lipid nanodisc, although visible at low contouring of the map, shows poor quality and with no elongated and rod-like feature that could be attributed to transmembrane helices (Figure S7). The latch turn, a short helix protruding from the C-terminus of M4 and interacting with the lower part of the cys-loop, is not resolved. This shows that, in MSP1E3D1

nanodiscs containing brain lipid extracts, the TMD conformation of  $\alpha 7\Delta$ ICDcryo is heterogeneous among the selected particles, indicating structural flexibility.

In the published structures in detergent or nanodiscs<sup>6,7</sup>, the variable loop from the ICD was truncated but the two  $\alpha$ -helices MA and MX were kept and resolved, notably the MA helices of each subunit that form a tight quaternary pentameric bundle that could possibly rigidify the TMD. To check if the weak TMD resolution is due to our ICD truncation, we solved the structure of  $\alpha 7$ FLcryo, also with a 50-fold excess of C4 and adding 100 $\mu$ M nicotine to further stabilize the protein conformation (C4-Nic structure) (Figure 1 and S5, table S1). The resulting reconstruction reaches a resolution of 3.6 Å for the ECD/nanobody part but also features a disordered transmembrane domain. Still, extra density is visible below the TMD/nanodisc area, compatible with the presence of the bundle of MA helices (Figure S7). In the previous cryo-EM structures of  $\alpha 7$  obtained in saposin nanodiscs containing soy lipids/25% cholesterol, the TMD was built<sup>6</sup>. However, its local resolution was lower than that of the ECD, indicating that the flexibility of the TMD is a distinctive feature of the  $\alpha 7$  nAChR.

Our data nevertheless allow the model building of the  $\alpha 7$  ECD, including the first glycan linked to  $\alpha 7$  at Asn23 and Asn67 and two glycans on  $\alpha 7$  Asn110, in complex with C4. C4 adopts a classical immunoglobulin-like fold, despite lacking the canonical intra-sandwich disulfide bond (Figure S3). In both C4-Apo and C4-Nic structures, five nanobodies are bound in a similar way and form an additional ring above the ECD. We numbered the nanobody chains according to the  $\alpha 7$  subunits anticlockwise arrangement, i.e. C4-chainF ( $n$ ) sits above  $\alpha 7$ -chainA (principal subunit,  $n$ ), C4-chain G ( $n+1$ ) sits above  $\alpha 7$ -chain B (complementary subunit,  $n+1$ ). Each nanobody interacts mainly with the top of a principal  $\alpha 7$  subunit but also with the  $\alpha 7$  complementary subunit, and presents its CDRs facing the ECD. The axis of each nanobody  $\beta$ -sandwich is roughly perpendicular to the membrane, in an orientation close to that of the  $\beta$ -sandwiches of the  $\alpha 7$  ECDs, which also display an immunoglobulin-type fold. Nanobodies interact substantially with each other (see below), and, while monomeric in solution, they present here a 5-fold assembly. The detailed description of the receptor-nanobody and nanobody-nanobody interactions are provided in sections 4/ and 5/.

We then analysed the receptor global conformation by measuring deviations to known structures and looking at structural hallmarks conserved in the family (loop C capping, cys-loop motion). First, for the C4-Nic structure, C $\alpha$  Root-mean-square deviations (rmsd) calculations of the  $\alpha 7$  ECD shows that the C4-Nic structure aligns best with structures obtained in presence of agonists, with or without PNU (Figure 2 and S8, table S2). Superimposition of the core of the  $\alpha 7$   $\beta$ -sandwich nicely illustrates this point (Figure S8). Measurement of the Loop C capping (10Å for the Cys189<sub>A</sub>-Tyr117<sub>E</sub> distance), and of the cys-loop outward motion (11Å for the Cys127<sub>A</sub>-Ile168<sub>E</sub> distance) clearly shows values that are characteristic of active/desensitized rather than resting conformation (Loop C capping around 10Å vs 17 Å, cys-loop motion around 10Å vs 8Å, respectively).

In the five orthosteric sites of C4-Nic, we found an additional density in which we could confidently build a nicotine molecule (Figure 1 and 2). The pyrrolidine points downward, and its electropositive ammonium lies in a box made up of aromatic residues from loop A (Tyr92), B (Trp148), C (Tyr187, Tyr194) and D ( $n+1$  Trp54). The pyridine points upward and elicits contacts with the loop C (disulfide bridge Cys189-Cys190) and loop E ( $n+1$  Leu118). Similar poses of the agonist were found in the structure of heteromeric  $\alpha 4\beta 2$  and  $\alpha 3\beta 4$  nAChRs in complex with nicotine<sup>11,13,14</sup>, and in the  $\alpha 7$  nAChR in complex with the related alkaloid epibatidine<sup>6</sup>. These observations are consistent with a conformation of  $\alpha 7$  corresponding to an active, partially-active or desensitized conformation. Given that information about the TMD conformation is missing in our dataset, we cannot unambiguously distinguish between those possibilities.

For the C4-Apo structure, the  $\alpha 7$  ECD structure aligns best with that of the Bgt-nanodisc and apo-detergent structures (Figure 2 and S8), with notably an uncapped Loop C (17 Å for the Cys189<sub>A</sub>-Tyr117<sub>E</sub> distance) and no cys-loop outward motion (Cys127<sub>A</sub>-Ile168<sub>E</sub> distance below 9 Å). Those markers indicate that the C4-Apo structure shows a resting-like conformation of  $\alpha 7$ . This is best exemplified by the orthosteric binding site which is empty and displays a wide-open loop C (Figure 1). In the nanobodies region, comparison of C4-Apo and C4-Nic structures shows few conformational changes upon nicotine binding apart from a small motion of the apex of the nanobodies away from the pentameric axis (Figure S9).

In conclusion, with five C4 nanobodies bound to its ECD,  $\alpha 7$  adopts conformations similar to those observed in the absence of nanobody, namely a resting-like conformation in the absence of agonist, and an active/partially-active/desensitized-like conformation in the presence of nicotine. Therefore, C4 appears to be a neutral binder, preserving the nicotine-elicited reorganizations in Cryo-EM conditions.

### *3/ E3 alone stabilizes an agonist-elicited conformation in Cryo-EM structures*

We then solved the structure of  $\alpha 7\Delta$ ICDcryo with a 50-fold excess of the E3 nanobody, with and without 100 μM nicotine, with an overall resolution of 2.6 and 2.8 Å in the ECD/nanobody region, respectively, and low signal in the TMD (Figure 3, S10, S11). Five E3 molecules are bound, in a similar arrangement to the one seen for C4. E3 adopts the same overall fold than C4 with local variations.

The E3-Nic structure shows an ECD conformation very close to that of C4-Nic, including the five bound nicotine molecules, consistent with active/partially-active/desensitized conformations (Figure 2, 3, S8 and S9). Surprisingly, the conformation of the  $\alpha 7$  ECD in the E3-Apo structure also matches best the agonist-bound conformations, including Loop C capping and Cys-loop outward motion (Figure 2 and 3). At the orthosteric site, the conformations of all binding determinants resemble the ones seen in the E3-Nic structure. In the cavity, we found a well-defined small spherical density, which is located where the electropositive pyrrolidine ammonium would be. The density would be compatible with water, or more likely a cation such as Na<sup>+</sup> that may contribute, along with the binding of E3, to compact the orthosteric site in the absence of nicotine (Figure 3). Yet, Cα rmsd calculations show that E3-Apo slightly differs from both E3-Nic and C4-Nic, with locally 1-2 Å deviations in the loop C, as well as the top and bottom regions of the ECD (Figure S9). In addition, we could observe a slight expansion of the ECD subunit in E3-Nic vs E3-Apo (~1 Å displacement), a motion comparable with the one observed between the Epi vs Epi/PNU structures in nanodiscs (PDB 7KOQ and 7KQX, Figure S9) but absent between the EVP and EVP/PNU structures in detergent (PDB 7EKP and 7EKT). As seen with C4, nicotine binding triggers a small motion of the tip of the nanobody away from the channel axis (Figure S9).

In conclusion, our data point to a striking effect of E3, which, in the cryo-EM conditions (high 50 μM E3 concentration, 1 hour equilibration period before freezing in the grids) stabilizes by itself an agonist-bound conformation through long-range allosteric interactions initiated at the top of the receptor. This suggests that, in electrophysiology, high E3 concentrations and long incubation periods could also trigger activation and/or desensitization in the absence of orthosteric agonist. However, such conditions are hardly reachable in a TEVC experiment. In addition, the fast desensitization of  $\alpha 7$  could mask a slow gradual activation by E3. To overcome these issues, we used the  $\alpha 7$  mutant L247T that disrupts a central hydrophobic ring in the channel<sup>15,16</sup> (Figure 6). This mutant strongly reduces desensitization and produces a marked gain of function phenotype increasing the efficacy of partial agonists. We recorded L247T currents elicited by 0.3 μM ACh before and after a 10 sec pre-application of 10 μM of E3. As expected, ACh-gated currents are potentiated by E3 pre-application (2.4 ± 1.1 fold). In addition, we observed an increase of the holding current during the pre-

application of E3 that represents  $6.0 \pm 1.8$  % of the response to  $0.3 \mu\text{M}$  ACh. This shows that E3 does have significant agonist properties in the absence of ACh when applied for a short period at a relatively high concentration on a weakly-desensitizing mutant.

#### 4/ Analysis of the E3 and C4 common epitope

C4 and E3 bind to  $\alpha 7$  in a highly similar manner (Figure 4 and S4), their CDRs contacting the top-ECD platform formed by the principal  $\alpha 7$  subunit down below (with a  $\sim 500 \text{ \AA}^2$  surface of interaction), and the complementary  $\alpha 7$  subunit ( $\sim 300 \text{ \AA}^2$ ). On the principal subunit, it is formed by the C-terminal half of the top  $\alpha$  helix that faces the vestibule, and by the long  $\beta 2$ - $\beta 3$  loop, also called Main Immunogenic Region (MIR)<sup>17</sup>, on the outer side. On the complementary subunit, it is formed by the N-terminal half of the top  $\alpha$ -helix.

Both nanobodies display unique disulfide bond patterns. First, E3 harbours the “canonical” disulfide bond that links the strands that just precedes the CDR1 and CDR3, which is missing in C4. Second, the CDR3 of E3 is longer by two residues, and is bent upwards by the presence of an extra disulfide bond between the end of the CDR3 and the second  $\beta$ -strand of the framework region 3 (FR3) (Figure S3). In known nanobodies featuring a long CDR3, a supplementary disulfide bond rigidifying the structure is common<sup>18</sup>. For both nanobodies, conserved side chains from the three CDRs (His32<sub>CDR1</sub>, Trp54<sub>CDR2</sub>, Arg101<sub>CDR3</sub> and Phe102<sub>CDR3</sub>, C4 numbering) are directly plunging into a groove bordered by the helix and MIR elements. Both nanobodies elicit a complex pattern of interactions with  $\alpha 7$  that is detailed in tables S3 and S4. Although the sets of interactions are different in C3 and E4, they involve conserved residues from the CDR1, CDR2 and first half of CDR3 (Gly27<sub>CDR1</sub>, Tyr33<sub>CDR1</sub>, Trp54<sub>CDR2</sub>, Arg101<sub>CDR3</sub>, Phe102<sub>CDR3</sub>, C4 numbering). They involve also non-conserved residues from the second half of the CDR3, where C4 residues Asp109 and Ser111 are engaged in an extensive set of interactions with the principal N-terminal helix, while much fewer contacts are found in E3 (Figure 4, tables S3 and S4). In addition, E3 shows a unique interaction between the Arg56<sub>CDR2</sub> guanidinium and both the main chain carbonyl and the first glycan grafted on  $\alpha 7$ Asn23 (pre- $\beta 1$ ), an interaction absent in C4 that harbours an alanine in place of the arginine at this position (Figure 3). Overall, the CDR3 is the main interacting loop, contacting the MIR and the N-ter helices of both subunits.

We further investigated the contribution of specific  $\alpha 7$  motifs to nanobody binding by mutagenesis of  $\alpha 7$ FLcryo. On the one hand, we mutated the charged residues of the Nter helix of  $\alpha 7$  (R4Q K5Q K9Q triple mutant and E9Q K12Q N13A triple mutant), and on the other hand we replaced the MIR residues to the aligned MIR of the  $\alpha 3$ -nAChR which does not bind C4 and E3<sup>9</sup>. Finally, we prevented N-linked glycosylation by mutating the serine of the Asn-X-Ser motif (Ser25Ala). We performed immunofluorescence assays in non-permeabilized HEK293 cells (Figure S4). Immunolabelling of the extracellular C-terminal Rho1D4 tag show that the MIR and glycosylation mutants are expressed at the cell surface, while mutants of the Nter helix are not. Immunolabelling with E3 and C4, using nanobodies fused to the heavy chain fragment of a human IgG (constructs detailed in<sup>9</sup>, Figure S4), show clear labelling of cells expressing the WT and glycosylation mutant, but no labelling of the MIR mutant. This confirms that the MIR is essential for the nanobody binding, while the glycosylation on Asn23 is not mandatory for E3 high-affinity binding.

#### 5/ Inter-nanobody interactions

A striking feature of the structures of  $\alpha 7$  bound to C4 and E3 is the 5-fold assembly adopted by the nanobodies above the receptors (Figures 1 and 3), where the FR3 region of each C4/E3 interacts with the FR1 region of the  $n+1$  C4/E3 nanobody through a  $\sim 200 \text{ \AA}^2$  interface (Figure S8). In C4, Tyr60, Ser63 and Lys 66 contact  $n+1$  Gln2 and Gln4 (Figure 5) and in E3,

Asn62 and Lys65 contact n+1 Gln3 and Gln5 and Gln 116. The CDR3 of E3 also contributes to the interface, the guanidinium of Arg108 lying near the carboxylate of Asp 113 suggesting a salt-bridge interaction. A more extensive set of inter-nanobody interactions is thus observed in E3 vs C4.

To further explore the quaternary binding mode of the nanobodies, we solved the structure of  $\alpha 7$ ICD<sub>cryo</sub> in the presence of a sub-saturating concentration of C4 (10 $\mu$ M) (Figure 5 and S11; Table S1). Indeed, in the early stages of the cryoEM work at the 2D classification step, we noticed that, for both E3 and C4, addition of 10 $\mu$ M of nanobodies is not sufficient to reach the C5-symmetry in the nanobody regions, indicating partial nanobody binding (Figure S13). We processed a dataset obtained with 10 $\mu$ M of C4 and no nicotine. 2D class averages show a minor fraction of particles containing one or two bound nanobodies, and a major fraction containing three bound nanobodies. We selected these later particles to solve a C4<sub>partial</sub>-Apo structure. Without imposed symmetry, we obtained a final volume of 4.4 Å resolution and, after density modification in Phenix<sup>19</sup>, we built a model with an overall model-versus-map resolution of 3.4 Å, where the main chains and most of the side chains of the  $\alpha 7$  ECD and the three nanobody molecules are confidently built. For simplicity, we labelled the three C4 according to their position in C4-Apo: C4 chains F, G and I sit above  $\alpha 7$  chains A, B and D, respectively. Interaction determinants of the three C4s with  $\alpha 7$  are identical to the ones observe in C4-Apo. C4<sub>F</sub> and C4<sub>G</sub> interact with each other in a similar manner than in C4-Apo, although through a slightly larger interaction surface (~260 Å<sup>2</sup>, Figure S8), while C4<sub>I</sub> sits alone.

Interestingly, each C4 chain displays a different radial and lateral inclination. The F, G and I chains are more inclined toward the vestibule (radial angles of 129.3°, 128.8° and 126.0°, respectively), compared to C4-Apo and C4-Nic (133.4° and 133.8°) (Figure S13). Likewise, the F, G and I chains are more inclined toward the (n+1) adjacent subunit (lateral angles of 82.8°, 80.5° and 78.2°, respectively), compared to C4-Apo and C4-Nic (85.1° and 85.3°). Therefore, data show that the nanobodies can bind independently from each other but that their orientation is constrained by the presence of neighbouring nanobodies. This suggests a sequential binding mode, where a single bound nanobody adopts a marked inclination toward the vestibule and the (n+1) adjacent  $\alpha 7$  subunit, where two adjacent nanobodies show intermediate inclinations, and five bound nanobodies adopt a straighter binding orientation. This later is necessary for the  $\alpha 7$  receptor to accommodate five bound nanobodies without steric clashes, eventually generating a symmetrical bundle (Figure 5).

#### 6/ E3-elicited potentiation involves interaction with Asn23-linked glycan

The Cryo-EM structures show a sticking allosteric action of E3, a feature that parallels its PAM activity in electrophysiological experiments. In contrast, C4 appears “silent” with both techniques. We thus investigated whether specific E3- $\alpha 7$  contacts are involved the PAM activity. To his aim, we compared the E3 and C4 co-structures, searching for specific motifs/interactions of E3 absent in C4, followed by mutational and functional assays.

First, to investigate a possible contribution of the CDR3 conformation of E3, we removed the extra disulfide bond in the C95S/C114V E3 mutant, but its displays unaltered potentiating effect in TEVC (Figure 6).

Second, a key feature of both nanobodies is their binding to the n+1 nanobody and  $\alpha 7$  subunit. Since  $\alpha 7$  undergoes a substantial quaternary reorganization during gating, the interaction of E3 with the complementary chains could contribute to constrain the relative arrangement of two adjacent  $\alpha 7$  subunits toward an active/desensitized conformation. We mutated specific potential salt bridges between E3 and E3(n+1) (Arg108-Asp113), as well as between E3 and  $\alpha 7$ (n+1) (Glu110-Lys8 <sub>$\alpha 7$ n+1</sub>). E3-R108Q and E3-E110Q show an intact

affinity by SPR, and a slightly weaker, yet not significantly different from E3, PAM activity by TEVC (Figure 6 and S4).

Third, a unique feature of E3 is the interaction between Arg56<sub>CDR2</sub> and the first sugar moiety linked to Asn23 from the principal subunit. We showed in mutating  $\alpha$ 7S25A that the glycosylation is not mandatory for E3 high-affinity binding. Interestingly,  $\alpha$ 7S25A is no more potentiated by E3, suggesting a key contribution of the first sugar moiety in potentiation. However, we cannot exclude that the mutation, although qualitatively showing binding in immunofluorescence, could decrease the affinity for E3 to such an extent that weak binding would occur in our electrophysiological assay (1  $\mu$ M E3). To address this issue, we tested the E3-R56A mutant. It shows an affinity identical to that of E3-WT in SPR (Figure S4), and almost totally loses its ability to potentiate ACh-gated currents in electrophysiology (Figure 6 and S4).

In conclusion, data pinpoint an Arg-sugar interaction at the E3- $\alpha$ 7(n) interface which mutation strongly decreases the potentiation, and two putative salt-bridges at the E3- $\alpha$ 7(n+1) and E3-E3 interfaces whose mutation show a tendency to decrease the potentiation.

## Discussion

In this study we solved five structures of the  $\alpha$ 7-nAChR in complex with two allosteric nanobodies, unravelling a common epitope at the apex of the receptor which is formed by the MIR and the N-terminal helices from two adjacent subunits. In the pLGIC family, nanobodies were previously generated and used mainly to assist structural determination. Most bind at the ortho- or pseudo-ortho-steric site in the 5HT<sub>3</sub>R<sup>20</sup>, GABA<sub>A</sub>R<sup>21,22</sup> and prokaryotic homolog ELIC<sup>23</sup>, except for a single NAM nanobody binding in the vestibule of ELIC<sup>23</sup>. It is noteworthy that E3 and C4 were generated through immunization of alpacas with cells expressing the fully glycosylated  $\alpha$ 7-nAChR ECD, while previous nanobodies involved immunization with purified proteins partly depleted from N-linked glycosylation by enzymatic cleavage (5HT<sub>3</sub>R) or production in GntI- cells (GABA<sub>A</sub>R). Interestingly, the unsharpened map of the E3/C4-bound structures suggests that glycosylation trees could substantially mask the orthosteric site, thereby plausibly preventing the generation of binders targeting this site and favouring a more apical epitope. Of note, the epitope of C4 and E3 shows weak sequence conservation among the various nAChR subtypes, accounting for their high specificity to the  $\alpha$ 7-nAChR with no observed binding by immunofluorescence to the  $\alpha$ 4 $\beta$ 2 and  $\alpha$ 3 $\beta$ 4 nAChRs<sup>9</sup>.

Several Fab fragments of conventional IgG were also found to bind within or around the orthosteric and pseudo-orthosteric sites in GABA<sub>A</sub>R<sup>24,25</sup> and  $\alpha$ 4 $\beta$ 2 nAChR<sup>13</sup>. More importantly, the MIR was first identified in the  $\alpha$ 1 subunit of the muscle-type nAChR as a key epitope for autoantibodies causing *myasthenia gravis*<sup>17,26</sup>. The crystal structure of the monomeric ECD of  $\alpha$ 1 in complex with a Fab fragment of one of those autoantibodies shows a binding mode involving interaction of both Fab chains with the MIR and the N-terminal helix of  $\alpha$ 1<sup>27</sup>. A somewhat similar binding mode is seen for an anti- $\alpha$ 3 Fab in complex with the  $\alpha$ 3 $\beta$ 4 nAChR<sup>14</sup>. However, both structures show a pose of the antibodies tilted to the edge of the top-ECD platform, the epitope centred on the MIR rather than the groove formed between the Nter helices and the MIR, as seen with E3 and C4. Therefore, the epitope of E3 and C4, while containing the MIR region, is unique among those so far characterized in pLGICs.

A unique feature of C4- and E3-bound structures is also the “pentamerization” of the nanobodies when binding to the  $\alpha$ 7 template. The C4partial-Apo structure shows that C4 binds in a sequential manner, a process requiring significant reorganization (change of radial and lateral inclination) of already bound nanobodies to accommodate new ones. Interestingly, SPR shows that C4 displays 0.1 nM affinity with an evaluated maximal occupation of 3 nanobodies per pentamer. In contrast, Cryo-EM experiments show that 10  $\mu$ M of C4 is not sufficient to

saturate the receptor, full saturation requiring a 50  $\mu\text{M}$  concentration. Data thus suggest that, within  $\alpha 7$  pentamers, the first binding events display high affinity (nanomolar from SPR) while the last binding events would display micromolar affinity. We suggest that the sequential binding mode, where the binding of nanobodies is impaired when adjacent positions are already occupied, might cause this negative cooperativity. This mechanism might also apply to E3 which displays similar difference in SPR vs Cryo-EM nanobody binding features.

Cryo-EM and TEVC experiments provide compelling evidence for a strong allosteric effect of E3, but not of C4. In this line, removal of the sugar linked to Asn-23, that contributes to the E3 but not to the C4 epitope, strongly impairs the PAM activity of E3 by TEVC. This indicates that the binding of E3 to the top platform drives both 1/ the potentiation of ACh-elicited currents on the WT  $\alpha 7$  and 2/ the stabilization of the active/desensitized state in the absence of orthosteric agonist, as seen in Cryo-EM and on the  $\alpha 7$ -L247T mutant. The PAM activity of E3, evaluated by potentiation of current elicited by 30  $\mu\text{M}$  of ACh, is maximal above 1  $\mu\text{M}$  with an apparent  $\text{EC}_{50}$  around 100 nM. SPR measure an affinity of 1 nM, suggesting that several binding events might be required to detect a PAM activity. In contrast, low  $\mu\text{M}$  concentrations of E3 are not sufficient to detect a direct agonist action. We show that 10  $\mu\text{M}$  E3 alone weakly but significantly activates the  $\alpha 7$ -L247T mutant, and that 50  $\mu\text{M}$  E3 alone drives  $\alpha 7$  into an active/partially-active/desensitized conformation in cryo-grids. Direct action of E3 is thus likely elicited by near-complete or complete saturation of the binding sites on the  $\alpha 7$  pentamer.

E3 mediates allosteric effects through its binding at the top platform of the receptor. Beside the orthosteric site, the  $\alpha 7$  nAChR is known to carry allosteric sites at the TMD, binding notably ivermectin<sup>28</sup> and PNU<sup>5,7</sup>, at the ECD-TMD interface where calcium binds<sup>29</sup>, and at a vestibular site located nearby the orthosteric site, that binds small fragments<sup>30</sup>. In the pLGIC family, another allosteric site is well established, the binding site of AM-3607, a PAM binding between the top platform and the orthosteric site of the  $\alpha 3$ GlyR<sup>31</sup>. Thus, the allosteric site targeted by E3 is unique and involves a large surface involving multiple contacts. E3 is strongly anchored in the principal  $\alpha 7$  subunit down below, with bulky side chains plunging into a groove bordered by the MIR and the helix. The PAM activity is strongly impaired by disrupting a key polar interaction with a sugar from the principal subunit nearby the interface with the complementary subunit, and possibly two putative salt bridges with the complementary n+1 E3 and  $\alpha 7$  subunit. We speculate that the binding of E3 constrains the relative arrangement of the principal and complementary subunits of  $\alpha 7$ , favouring a subunit tilt associated with gating (Figure 7). Therefore, E3 implements a novel allosteric site which is the most remote from the core of the coupling pathway between the orthosteric site and the activation gate of the channel.

In conclusion, our work reveals a unique mechanism where nanobodies prolong the length of the pentameric architecture of the ECD to control the global allosteric conformation of the receptor. The modular architecture of pLGICs, made up of ECD and TMD domains that fold in a partially autonomous way<sup>32–34</sup>, is thus artificially extended here by an extra-module that tightly binds and is allosterically coupled to the native receptor. Such a regulation by additional modules is reminiscent of receptors carrying a regulatory N-terminal domain such as the pLGIC Declic<sup>35</sup>, or the tetrameric glutamate receptors. Finally, from a pharmacological perspective, E3 constitutes an original and highly subtype-specific therapeutic antibody candidate for  $\alpha 7$ -linked pathologies, including autoimmune<sup>36</sup>, neurodegenerative or psychiatric diseases.

## Methods

### *Lentiviral vectors construction and production*

The lentiviral transfer plasmid was generated from the pHR-CMV-TetO2-IRES-EmGFP and pHR-CMV-TetO2-IRES-mRuby2 plasmids available on Addgene. Human cDNA for  $\alpha 7$ -nAChRs and NACHO inserts were cloned using In-fusion cloning kit (Takara). After cloning in the lentiviral transfer plasmids, genes are preceded by a CMV promoter and a tet repressor element (CMV-TetO2) and followed by an IRES element promoting the expression of GFP (IRES-GFP,  $\alpha 7$ ) or mRuby (IRES-Ruby, Nacho).

Viral particles were generated by co-transfection of HEK-293T cells by the lentiviral transfer plasmid, a packaging plasmid and an envelope plasmid. Two days after transfection, viral particles were harvested in the supernatant, treated with DNaseI, filtered through 0.45  $\mu$ m pores, concentrated by ultracentrifugation and resuspended in PBS. Viral stocks were stored in small aliquots at  $-80^{\circ}\text{C}$  before use. Viral titres were estimated by quantification of the p24 capsid protein using HIV-1 p24 antigen immunoassay (ZeptoMetrix) and by Fluorescence Activated Cell Sorting (FACS).

### *Lentiviral transduction, inducible expression in Trex cells*

A mixture of  $\alpha 7$ -containing and NACHO-containing lentiviral particles (10:1) was used to transduce HEK T-Rex 293 cells (ThermoFischer). The resulting inducible cell line was cultured in suspension flasks in Freestyle 293 expression medium supplemented with blasticidin (5-10  $\mu\text{g}/\text{ml}$  final) and FBS (1%) in an orbital incubator at  $37^{\circ}\text{C}$  and 8%  $\text{CO}_2$ . Protein expression was induced at a density of  $3\text{-}4 \times 10^6$  cells /ml by addition of doxycycline (10  $\mu\text{g}/\text{L}$  final). The cells were further cultured for 48h before harvesting by centrifugation.

### *$\alpha 7$ -nAChR purification*

After low-speed centrifugation, the pellet was washed with cold PBS 1x and centrifuged again. Cells were resuspended in buffer A (20mM Tris pH8.0, 250mM NaCl) supplemented with antiprotease cocktail and mechanically lysed (Ultra-turrax T20, IKA, 9x30 seconds). Lysed cells were centrifuged at low speed (2000g) to remove debris and intact cells and membranes were collected by ultracentrifugation (190000g for 2 hours). All further steps were carried out at  $4^{\circ}\text{C}$ . Membranes were mechanically broken and were resuspended in buffer A (10ml of buffer per gram of membrane) and supplemented with 1% w/v final of dodecyl-maltoside (DDM, Anatrace) for 1h solubilization under gentle stirring. The insoluble material was removed by ultracentrifugation (190000g for 45 minutes). The supernatant containing solubilized proteins was bound overnight at  $4^{\circ}\text{C}$  on a gravity flow Rho1D4 resin (Cube Biotech) equilibrated with buffer A supplemented with 0.05% DDM. After binding overnight, resin was washed with buffer A and 0.05% DDM and gradually washed to remove DDM and exchanged for 0.01 % Lauryl Maltose Neopentyl Glycol (LMNG, Anatrace).

MSP1E3D1-Histag plasmid was obtained from Addgene, and protein was purified as described in Ritchie *et al* 2009. Porcine Brain Lipids Total extracts (BLT, Avanti) were resuspended in buffer A containing 0.01% LMNG at 10mM, sonicated and stored at  $-80^{\circ}\text{C}$  until use.

The  $\alpha 7$  receptor on its resin was incubated with MSP1E3D1 and BLT extracts (ratio 1:2:200) for 1h at  $4^{\circ}\text{C}$ . The removal of detergent was initiated by the addition of bio-beads (BioRad) twice for 1h at  $4^{\circ}\text{C}$ . The receptor-lipidic disc mixture was washed in buffer without DDM and was eluted with 500  $\mu\text{M}$  Rho1D4 peptide (Cube biotech) for 4x1hour at  $4^{\circ}\text{C}$ . The receptor-lipidic disc mixture was concentrated to 300-400  $\mu\text{l}$ . Polishing was done with a binding on a cobalt resin for 15min at  $4^{\circ}\text{C}$ , washed with buffer A and was eluted with 250mM of imidazole. The fractions were pooled and concentrated to 1-5  $\mu\text{M}$ . Imidazole was removed by washing at concentration step.

### *Nanobodies purification*

Genes coding for C4 and E3 nanobodies (and E3 mutants) with cMyc tag and 6xHis-tag at the nanobody's C-terminal were cloned into a pFUSE-derived vector (InvivoGen). The vector was used to transform Expi293F mammalian cells (ThermoFisher), and protein expression was carried out according to manufacturer's recommendations using 100 ml final volume of cells suspension. Protein was then purified from the expression medium by affinity chromatography on a 1 mL HiTrap TALON crude column (Cytiva). After sample application, the column was first washed with 10 column volumes of PBS and 10 column volume of PBS supplemented with 10 mM Imidazole (pH=7.4) (Sigma), the protein was subsequently eluted with 5 column volumes of PBS supplemented with 0.5 M Imidazole (pH=7.4). Affinity-eluted nanobodies were finally polished on a HiLoad 16/600 Superdex 200pg Pre-packed column (Cytiva) using PBS buffer.

### *Cryo-EM Sample Preparation*

Typical grids were prepared with 1 $\mu$ M  $\alpha$ 7 pentamer supplemented with 10 or 50 $\mu$ M of nanobodies and 100 $\mu$ M nicotine when applicable. For preparation of cryo-EM grids, UltrAuFoil grids 300 mesh 1.2/1.3 or 0.6/1.0 from Quantifoil were glow discharged in a PELCO easiGlow for 25mA/15s. Three  $\mu$ l of protein were applied to grids before blotting for 6s at 100% humidity and 10°C. Grids were plunge-frozen with a Vitrobot Mark-IV (ThermoFisher). Frozen grids were stored in liquid nitrogen until use.

### *Data collection, processing and model building*

Datasets were collected on a ThermoFisher Glacios equipped with a Falcon 4i detector at Institut Pasteur, or a ThermoFisher Titan equipped with a Gatan energy filter bioquantum/K3 at Institut Pasteur or on a ThermoFisher IC-Krios equipped with a SelectrisX and a Falcon4i detector at EMBL-Heidelberg. All datasets were acquired in counting mode using EPU (ThermoFisher) or SerialEM (see Table supp 1 and Figures S4, S5, S9, S10, S11 for datasets specific details). The beam-induced motion was corrected by MotionCor2 and defocus values were estimated by CTFFIND-4.1. Laplacian-of-Gaussian algorithm from Relion4 or blob-picker from CryoSPARC3.3.2 were used to pick particles that were submitted to 2D classification. 2D classes showing landmark secondary structures of  $\alpha$ 7-nAChR were used to pick again particles. After two rounds of 2D classification, classes with clear secondary structures characteristic of  $\alpha$ 7 were selected as the initial pool of particles used for further processing. Unsymmetrized initial model was built in Relion4, symmetrized in C5 (or unsymmetrized in the case of C4partial) and used for Relion4 unsupervised 3D classification with a 60 Å initial low-pass filter. When indicated, an additional 3D classification without alignment was performed. The final pool of particles was used for 3D refinement in Relion4 with C5-symmetry imposed and relaxed in C1 to account for local heterogeneity, using a mask that includes signal we assigned to the transmembrane domain. FSC plots were calculated using the post-processing tool from Relion4.

Maps from the refinement runs were sharpened in Phenix1.20, except for the C4partial-Apo volume that was subjected to Phenix1.20 density modification using an initial model made with C4-Apo depleted in two nanobodies molecules. Low sigma value allows to visualize the transmembrane and intracellular regions, but they disappear at sigma values compatible with model building. On the first processed dataset (E3-Nic) molecular replacement tool from Phenix1.20 using the ECD of the Epi-bound nanodisc structure (PDB 7KOQ) was used to place  $\alpha$ 7. Phenix1.20 chain tracing was used to *de novo* build the five E3 molecules from their amino-acids sequence, except for the C-terminal Histag that is flexible and form a poorly resolved

density on the apex of the structure. Model was modified in Coot and refined in Phenix1.20 using secondary structure and Ramachandran restraints. Using the glycosylation tool from Coot we were able to build the first sugars of the glycosylations on Asn23 and Asn67 and two sugars on Asn110 but densities suggest denser glycosylation trees. The two cysteine disulfide bonds in E3 were well resolved, as was the one in the  $\alpha 7$  Cysloop. However, the two cysteines side chains from the canonic disulfide bond of the C-loop (Cys189/Cys190), although well resolved, do not appeared bond in the density. This loop is exposed to the solvent and the disulfide bond is known to be sensitive to radiation damage (Rhaman et al, Noviello et al, Hattne et al 2018), we thus omitted the bond in the structure. For the remaining datasets, the resulting E3-Nic structure was used for molecular replacement, sequence of the nanobodies was further adjusted for C4 and structures were refined using Coot and Phenix and validated using the MolProbity Phenix validation tool.

Structure analysis was performed using Pymol, ChimeraX and PISA from the CCP4 suite.

### *Real-time surface plasmon resonance assays*

SPR assays were performed on a Biacore T200 instrument (Cytiva) equilibrated in buffer A pH8 at 25°C.

Surface preparation: Carboxy-methylated dextran CM5 sensorchips (Cytiva) were functionalized by immobilizing covalently the anti-Rho tag monoclonal antibody 1D4 (50 $\mu$ g/ml at pH4) through amide bonds at a density of 13000-15000 resonance units (RU, 1RU $\approx$ 1pg/mm<sup>2</sup>).  $\alpha 7$ -nanodiscs (10 $\mu$ g/ml) were then captured on the 1D4 surfaces at a density of 1300-1500RU.

Binding assays: the association and dissociation kinetic properties of nanobodies/ $\alpha 7$  complexes were determined by injecting nanobodies in single cycle kinetics mode (five increasing concentration injections of 600s each at 30 $\mu$ l/min on both  $\alpha 7$ /Rho1D4 and reference Rho1D4-only surfaces. This was followed by a final dissociation phase of 1800s. Three-fold dilution series were used for each nanobody (100-1.23 nM and 20-0.25nM for E3 and its mutants; 6.66-0.08nM for C4). The specific SPR signals were analysed using the Biacore T200 evaluation software (Cytiva) yielding association ( $k_{on}$ ) and dissociation ( $k_{off}$ ) rates, and equilibrium dissociation constants ( $K_d$ ) for each nanobody/ $\alpha 7$  complex.

### *Immunofluorescence*

HEK293 cells were cultured on poly-D-lysine (Millipore) coated glass coverslips, according to manufacturer's recommendations. The  $\alpha 7$ -nAChR-IRES-eGFP transfer plasmid or its mutated version ( $\alpha 3$ MIR or S25A) was co-transfected with NACHO, Ric-3 and SAT1 plasmids (1:1:1:1 ratio) using and the JetPrime transfection reagent (Polyplus), according to manufacturer instructions.

48h-36h after transfection, cells were fixed with 4% PFA and permeabilized for 2 min with a solution of ethanol/methanol (1:1). Non-specific binding was blocked with 10% BSA in PBS for 5 min at room temperature. The nanobodies-Fc constructs were diluted to 5 $\mu$ g/ml in 10% BSA in PBS and incubated with the coverslips for 2h at room temperature.

Proper expression of  $\alpha 7$ -nAChRs was verified by a mouse anti-Rho1D4. Anti-human IgG and anti-mouse IgG coupled to Alexa647 (ThermoFisher) were diluted in PBS-BSA.

Coverslips were mounted on slides after Prolong-DAPI staining (Invitrogen) and visualized using epi-fluorescence at constant exposure times. All experiments were reproduced  $\geq 4$  times.

### *Two-electrode voltage-clamp electrophysiology*

*Xenopus laevis* oocytes were obtained from EcoCyte Bioscience, Germany and from Tefor Paris-Saclay UAR2010 and maintained in modified Barth's medium (87.34 mM NaCl, 1 mM KCl, 0.66mM NaNO<sub>3</sub>, 0.75 mM CaCl<sub>2</sub>, 0.82mM MgSO<sub>4</sub>, 2.4 mM NaHCO<sub>3</sub>, 10 mM HEPES

pH 7.6). Defolliculated oocytes were submitted to intranuclear injection of ~2–6 ng of  $\alpha 7$ -nAChR-IRES-eGFP transfer plasmid and kept at 18 °C for 2–3 days before recording.

Recordings were performed with a Digidata 1550A digitizer (Molecular Devices), an Axon Instruments GeneClamp 500 amplifier (Molecular Devices), an automated voltage-controlled perfusion system which controls an 8-port and a 12-port electric rotary valves (Bio-Chem Fluidics) both connected to a 2-way 4-port electric rotary valve (Bio-Chem Fluidics) and the pClamp 10.6 software (Molecular Devices).

Oocytes were perfused with Ringer's buffer (100 mM NaCl, 2.5 mM KCl, 10 mM HEPES, 2 mM CaCl<sub>2</sub>, 1 mM MgCl<sub>2</sub>, pH 7.3). Nanobodies solutions were applied after dilution in Ringer's buffer and all currents were measured at –60mV. For all the experiments oocytes were perfused with Ringer's buffer for 30s, then 5s with 30 $\mu$ M ACh (or 0,3 $\mu$ M for L9'T) followed by 2- or 3-minutes wash and another 5s ACh application. The nanobody solution was then perfused for 30s (or 10s for L9'T) followed by 5s of 30 $\mu$ M ACh and 2- or 3-minutes wash and another 5s ACh application.

Recordings were analyzed using ClampFit and GraphPad Prism. Measurements were performed at the peak of the response. For the statistical comparisons using GraphPad Prism, we performed Student's *t test*.

## References

1. Nemezc, A., Prevost, M. S., Menny, A. & Corringer, P.-J. Emerging Molecular Mechanisms of Signal Transduction in Pentameric Ligand-Gated Ion Channels. *Neuron* **90**, 452–470 (2016).
2. Papke, R. L. & Horenstein, N. A. Therapeutic Targeting of  $\alpha 7$  Nicotinic Acetylcholine Receptors. *Pharmacol. Rev.* **73**, 1118–1149 (2021).
3. Hone, A. J. & McIntosh, J. M. Nicotinic acetylcholine receptors in neuropathic and inflammatory pain. *FEBS Lett.* **592**, 1045–1062 (2018).
4. Terry, A. V.  $\alpha 7$  nicotinic acetylcholine receptors as therapeutic targets in schizophrenia\_ Update on animal and clinical studies and strategies for the future. (2020).
5. Young, G. T., Zwart, R., Walker, A. S., Sher, E. & Millar, N. S. Potentiation of  $\alpha 7$  nicotinic acetylcholine receptors via an allosteric transmembrane site. *Proc. Natl. Acad. Sci.* **105**, 14686–14691 (2008).
6. Noviello, C. M. *et al.* Structure and gating mechanism of the  $\alpha 7$  nicotinic acetylcholine receptor. *Cell* **184**, 2121–2134.e13 (2021).
7. Zhao, Y. *et al.* Structural basis of human  $\alpha 7$  nicotinic acetylcholine receptor activation. *Cell Res.* 1–4 (2021) doi:10.1038/s41422-021-00509-6.
8. Zhuang, Y., Noviello, C. M., Hibbs, R. E., Howard, R. J. & Lindahl, E. Differential interactions of resting, activated, and desensitized states of the  $\alpha 7$  nicotinic acetylcholine receptor with lipidic modulators. *Proc. Natl. Acad. Sci.* **119**, e2208081119 (2022).
9. Li, Q., Nemezc, Á., Aymé, G., Prevost, M. S. & Pons, S. Generation of nanobodies acting as silent and positive allosteric modulators of the  $\alpha 7$  nicotinic acetylcholine receptor. Preprint at <https://www.biorxiv.org/>
10. Elegheert, J. *et al.* Lentiviral transduction of mammalian cells for fast, scalable and high-level production of soluble and membrane proteins. *Nat. Protoc.* **13**, 2991–3017 (2018).
11. Morales-Perez, C. L., Noviello, C. M. & Hibbs, R. E. X-ray structure of the human  $\alpha 4\beta 2$  nicotinic receptor. *Nature* **538**, 416–416 (2016).
12. Gu, S. *et al.* Brain  $\alpha 7$  Nicotinic Acetylcholine Receptor Assembly Requires NACHO. *Neuron* **89**, 948–955 (2016).

13. Walsh, R. M. *et al.* Structural principles of distinct assemblies of the human  $\alpha 4\beta 2$  nicotinic receptor. *Nature* 1–25 (2018) doi:10.1038/s41586-018-0081-7.
14. Gharpure, A. *et al.* Agonist Selectivity and Ion Permeation in the  $\alpha 3\beta 4$  Ganglionic Nicotinic Receptor. *Neuron* **104**, 501–511.e6 (2019).
15. Revah, F. *et al.* Mutations in the channel domain alter desensitization of a neuronal nicotinic receptor. **353**, (1991).
16. Bertrand, D. *et al.* Unconventional pharmacology of a neuronal nicotinic receptor mutated in the channel domain. *Proc. Natl. Acad. Sci.* **89**, 1261–1265 (1992).
17. Tzartos, S., Langeberg, L., Hochschwender, S. & Lindstrom, J. Demonstration of a main immunogenic region on acetylcholine receptors from human muscle using monoclonal antibodies to human receptor. *FEBS Lett.* **158**, 116–118 (1983).
18. Muyldermans, S. Single domain camel antibodies: current status. *Rev. Mol. Biotechnol.* **74**, 277–302 (2001).
19. Liebschner, D. *et al.* Macromolecular structure determination using X-rays, neutrons and electrons: recent developments in *Phenix*. *Acta Crystallogr. Sect. Struct. Biol.* **75**, 861–877 (2019).
20. Hassaine, G. *et al.* X-ray structure of the mouse serotonin 5-HT<sub>3</sub> receptor. *Nature* 1–21 (2014) doi:10.1038/nature13552.
21. Masiulis, S. *et al.* GABAA receptor signalling mechanisms revealed by structural pharmacology. *Nature* 1–22 (2018) doi:10.1038/s41586-018-0832-5.
22. Sente, A. *et al.* Differential assembly diversifies GABAA receptor structures and signalling. *Nature* **604**, 190–194 (2022).
23. Brams, M. *et al.* Modulation of the *Erwinia* ligand-gated ion channel (ELIC) and the 5-HT<sub>3</sub> receptor via a common vestibule site. *eLife* **9**, 213–19 (2020).
24. Noviello, C. M., Kreye, J., Teng, J., Prüss, H. & Hibbs, R. E. Structural mechanisms of GABAA receptor autoimmune encephalitis. *Cell* **185**, 2469–2477.e13 (2022).
25. Zhu, S. *et al.* Structure of a human synaptic GABAA receptor. *Nature* **559**, 67–72 (2018).
26. Luo, J. *et al.* Main Immunogenic Region Structure Promotes Binding of Conformation-Dependent Myasthenia Gravis Autoantibodies, Nicotinic Acetylcholine Receptor Conformation Maturation, and Agonist Sensitivity. *J. Neurosci.* **29**, 13898–13908 (2009).
27. Noridomi, K., Watanabe, G., Hansen, M. N., Han, G. W. & Chen, L. Structural insights into the molecular mechanisms of myasthenia gravis and their therapeutic implications. *eLife* **6**, e23043 (2017).
28. Krause, R. M. *et al.* Ivermectin: A Positive Allosteric Effector of the  $\alpha 7$  Neuronal Nicotinic Acetylcholine Receptor.
29. Galzi, J. L., Bertrand, S., Corringer, P. J., CHANGEUX, J. P. & Bertrand, D. Identification of calcium binding sites that regulate potentiation of a neuronal nicotinic acetylcholine receptor. *EMBO J.* **15**, 5824–5832 (1996).
30. Delbart, F. *et al.* An allosteric binding site of the  $\alpha 7$  nicotinic acetylcholine receptor revealed in a humanized acetylcholine-binding protein. *J. Biol. Chem.* **293**, 2534–2545 (2018).
31. Huang, X. *et al.* Crystal structures of human glycine receptor  $\alpha 3$  bound to a novel class of analgesic potentiators. *Nat. Struct. Mol. Biol.* **24**, 108–113 (2016).
32. Eiselé, J. L. *et al.* Chimaeric nicotinic-serotonergic receptor combines distinct ligand binding and channel specificities. *Nature* **366**, 479–483 (1993).
33. Nury, H. *et al.* Crystal structure of the extracellular domain of a bacterial ligand-gated ion channel. *J. Mol. Biol.* **395**, 1114–1127 (2010).
34. Moraga-Cid, G. *et al.* Allosteric and hyperekplexic mutant phenotypes investigated on an  $\alpha 1$  glycine receptor transmembrane structure. *Proc. Natl. Acad. Sci. U. S. A.* 201417864 (2015) doi:10.1073/pnas.1417864112.

35. Hu, H., Howard, R. J., Bastolla, U., Lindahl, E. & Delarue, M. Structural basis for allosteric transitions of a multidomain pentameric ligand-gated ion channel. *Proc. Natl. Acad. Sci.* **117**, 13437–13446 (2020).
36. Lykhmus, O. *et al.*  $\alpha 7$  Nicotinic Acetylcholine Receptor-Specific Antibody Induces Inflammation and Amyloid  $\beta 42$  Accumulation in the Mouse Brain to Impair Memory. *PLOS ONE* (2015).

## Acknowledgements

This work was supported by an ERC (Grant no. 788974, Dynacotine) to PJC and MSP, an Institut Pasteur Axe3 Seed grant to MSP, iNEXT-Discovery funding (PID: 22438) to MSP, the Foundation de la Recherche Médicale (Equipe FRM DEQ20140329497) to PJC, the Agence Nationale de la Recherche (Grant ANR-21-CE37-0026, Nicoptotouch) to PJC and GA, and the Institut National du cancer INCA to GBD. The authors thank the Nanoimaging Core Facility (Institut Pasteur) and Simon Fromm (EMBL-HD) for their precious help in data collection, and H. Nury, A. Menny and N. Wolff for discussions and critical reading of the manuscript.

## Competing interests

GA, PJC, PL, MP, NB are inventors of patent application US 63/383,099 that covers the VHH and therapeutic uses thereof.

## Authors contributions

MSP and PJC conceived and supervised the study. NB and SP prepared lentiviruses with UM supervision. PL and GA produced nanobodies. MSP and NB setup and performed protein production, cryoEM samples preparation and data collection. MG, GPA and FB helped in early biochemistry, electron microscopy and data processing respectively. MSP processed the cryoEM data and solved the structures. NB and PE performed SPR experiments. GDB performed electrophysiology experiments. All authors helped in the results analysis and interpretation. MSP and PJC wrote the manuscript with contributions from all authors.

## Figures

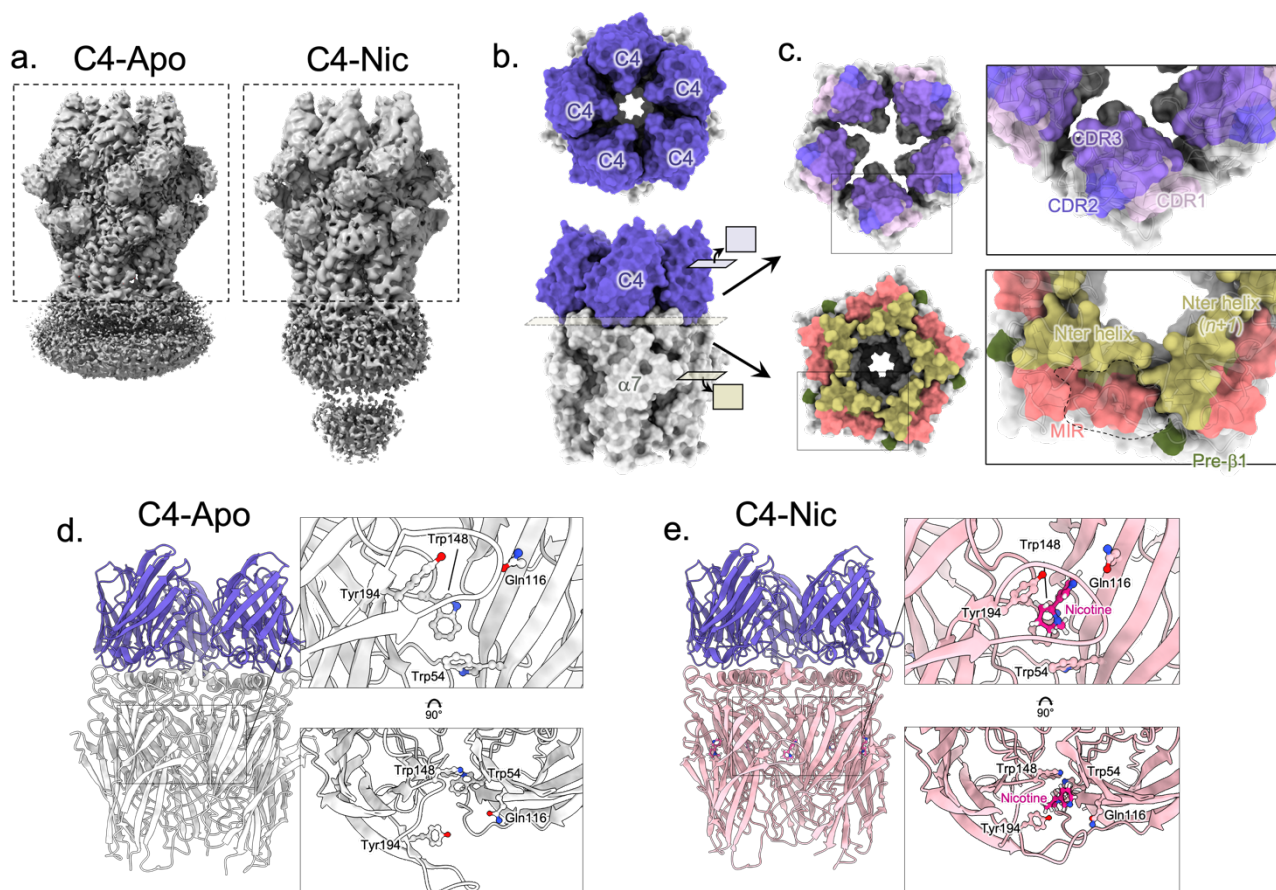


**Figure 1 : C4-α7 cryo-EM structures in the absence or presence of nicotine**

- Unsharpened maps of the  $\alpha 7 \Delta \text{ICD}$  cryo in complex with C4 (C4-Apo, left) and of the  $\alpha 7 \text{FL}$  cryo in complex with C4 and nicotine (C4-Nic, right) with densities contoured at 2σ. The dashed boxes denote the parts that were used for model building.
- Top and side views of the C4-Apo structure, protein chains are depicted in white ( $\alpha 7$  apo-) and purple (C4). The structure is shown exploded in c.
- Top : Bottom view of the ring of C4 with the molecular surface of the three CDRs colored in shades of purple. Bottom : Top view of the ECD of  $\alpha 7$  with Nter helices, MIR and pre-β1 colored in yellow, pink and green respectively. The groove in which the CDRs are plunging is delimited with a dashed line.
- Side view of the C4-Apo structure, represented in cartoon with  $\alpha 7$  in white and C4 in purple. The orthosteric binding site is enlarged and further rotated by 90°C in the right panels. Residues involved in nicotine binding are depicted in sticks.
- Side view of the C4-Nic structure, represented in cartoon with  $\alpha 7$  in pink and C4 in purple. The orthosteric binding site is enlarged and further rotated by 90°C in the right panels. Residues involved in nicotine binding and nicotine itself are depicted in sticks.

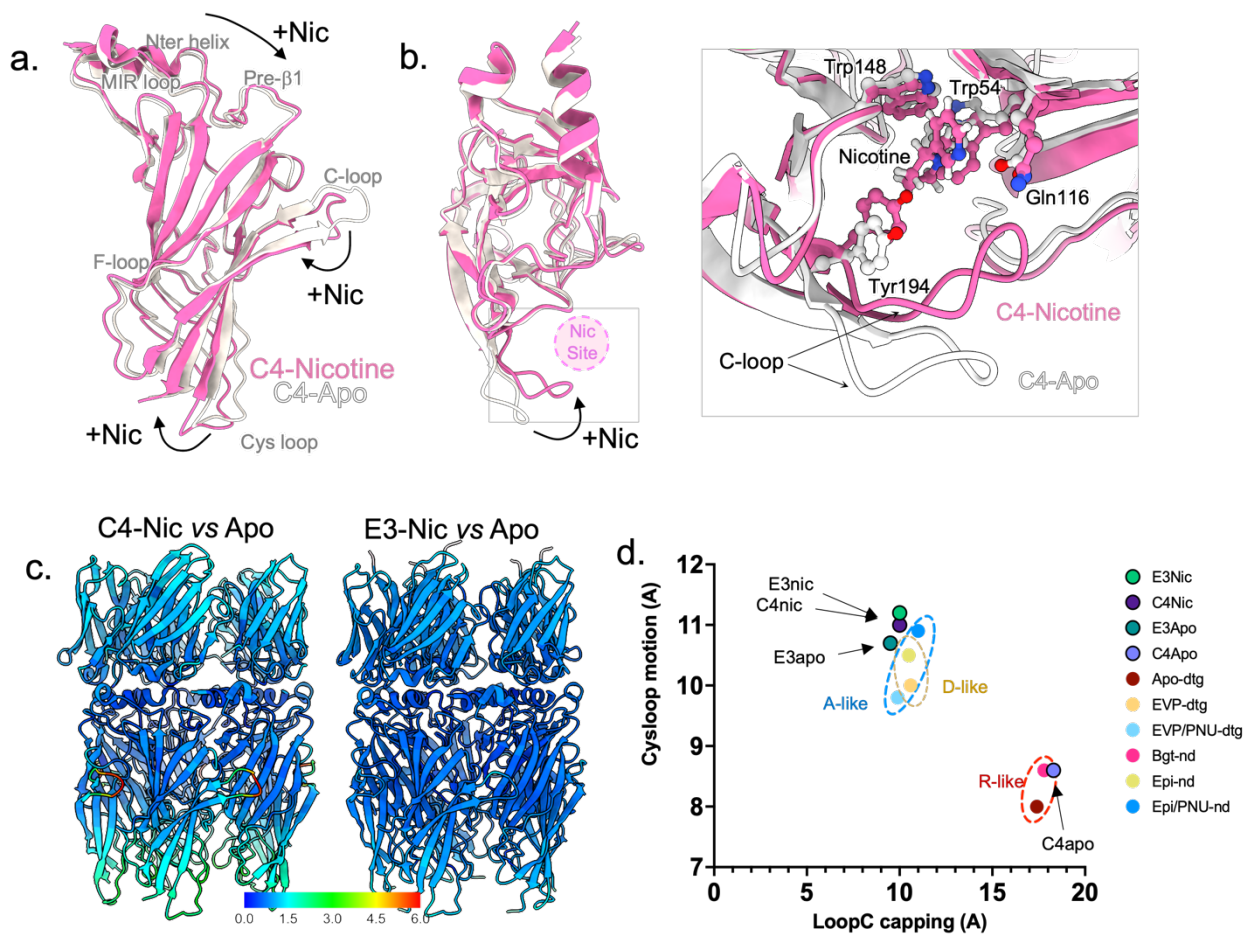


**Figure 2 :  $\alpha 7$  conformation in C4-Apo corresponds to a resting-like state, and in C4-Nic, E3-Apo and E3-Nic to a partially active/active/desensitized state.**

- $\alpha 7$  monomers from the C4-Apo (grey) and C4-Nic structure (pink) are seen from the side and depicted in cartoons after superimposition of the whole  $\alpha 7$  pentamer. Landmark loops are labelled and motions from Apo- to Nic- are highlighted with black arrows.
- The same representation than in a. but seen from the top. Nicotine binding site is depicted with a pink circle. A close view of the nicotine binding site is shown on the right. Nicotine and key residues from the binding pocket are labelled and depicted in sticks.
- Conformational changes upon nicotine binding in C4-bound (left) and E3-bound (right) structures. C4-Nic and E3-Nic are represented in cartoons and  $C\alpha$  are colored according to the rmsd value calculated using their Apo- counterpart, with the same range for both and shown in the color key below.
- Correlation of the cys-loop outward motion and Loop C capping in the known structures of  $\alpha 7$  allows to define pairs of values that are landmarks of the  $\alpha 7$  conformations. R, A, and D-like structures are grouped in dashed circles.

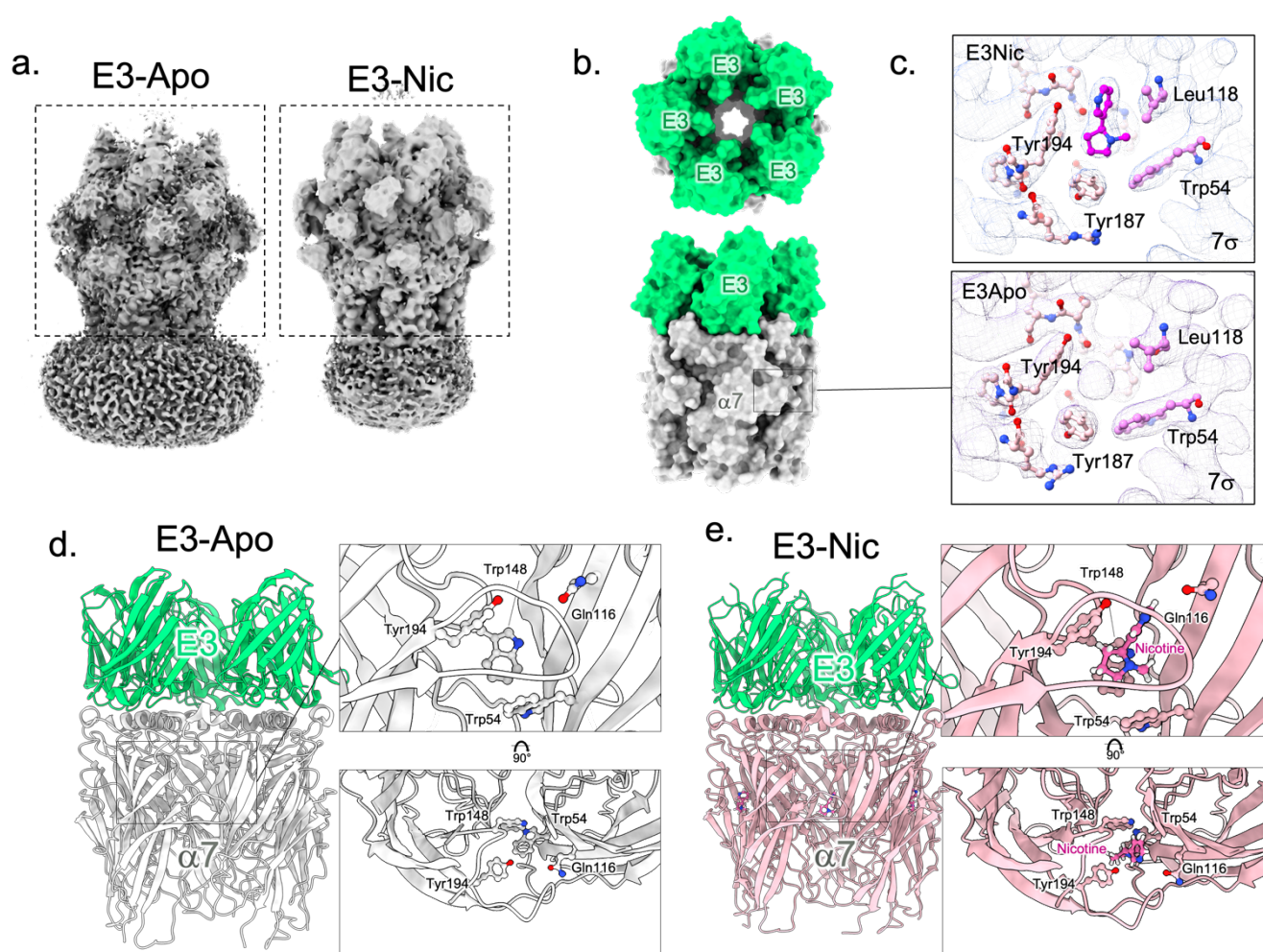


**Figure 3 : E3- $\alpha 7$  cryo-EM structures in the absence or presence of nicotine**

- Unsharpened maps of the  $\alpha 7$ ΔICD cryo-EM structure in complex with E3-Apo (left) and E3-Nic (right) with densities contoured at  $2\sigma$ . The dashed boxes denote the parts that were used for model building.
- Top and side views of the E3-Apo structure, protein chains are depicted in white ( $\alpha 7$  apo-) and green (E3). The orthosteric sites are shown in c.
- Neurotransmitter binding pocket of E3-Nic and E3-Apo. Electron densities are contoured at  $7\sigma$  and residues involved in neurotransmitter binding are shown in sticks. Nicotine was built in the extra density found in E3-Nic while the small and spherical density found in E3-Apo likely fits a cation or a water molecule.
- Side view of the E3-Apo structure, represented in cartoon with  $\alpha 7$  in white and E3 in green. The orthosteric binding site is enlarged and further rotated by  $90^\circ$  in the right panels. Residues involved in nicotine binding are depicted in sticks.
- Side view of the E3-Nic structure, represented in cartoon with  $\alpha 7$  in pink and E3 in green. The orthosteric binding site is enlarged and further rotated by  $90^\circ$  in the right panels. Residues involved in nicotine binding and nicotine itself are depicted in sticks.

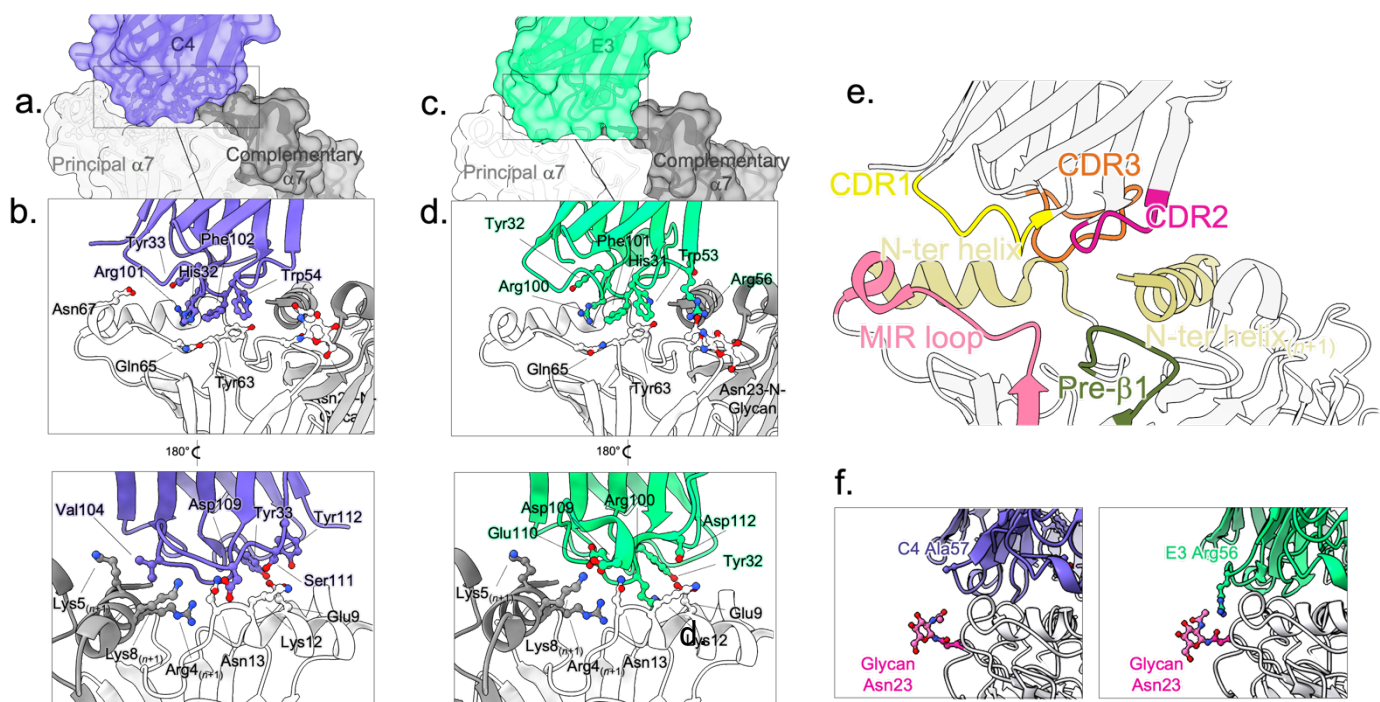


**Figure 4: Binding pose and epitope of C4 and E3.**

- Overview of the binding site of C4 on  $\alpha 7$  exemplified by the C4-Apo structure. One C4 molecule (purple surface and cartoon) contacts two  $\alpha 7$  subunits depicted in light (principal n subunit) and dark (complementary anticlockwise n+1 subunit) surface and cartoons.
- Details of the binding site as seen from the solvent (upper panel) or the vestibule (lower panel) of  $\alpha 7$  with color code as in a. Key residues are labeled, and their side chains are displayed in stick balls.
- Same as in a. but with the E3-Apo structure, E3 is colored in green
- Same as in b. but with the E3-Apo structure, E3 is colored in green.
- Overview of the loops involved in binding exemplified by the C4-Apo structure represented in cartoons.
- Interaction of E3 with Asn23 glycan. Close view of the Glycan (pink sticks) built on  $\alpha 7$ -Asn23 (pink sticks) from the pre- $\beta 1$  of  $\alpha 7$  (grey) and of the CDR2 of C4 (left, purple) or E3 (right, green). Ala57 from C4 and its homologous Arg56 from E3 are depicted in sticks.

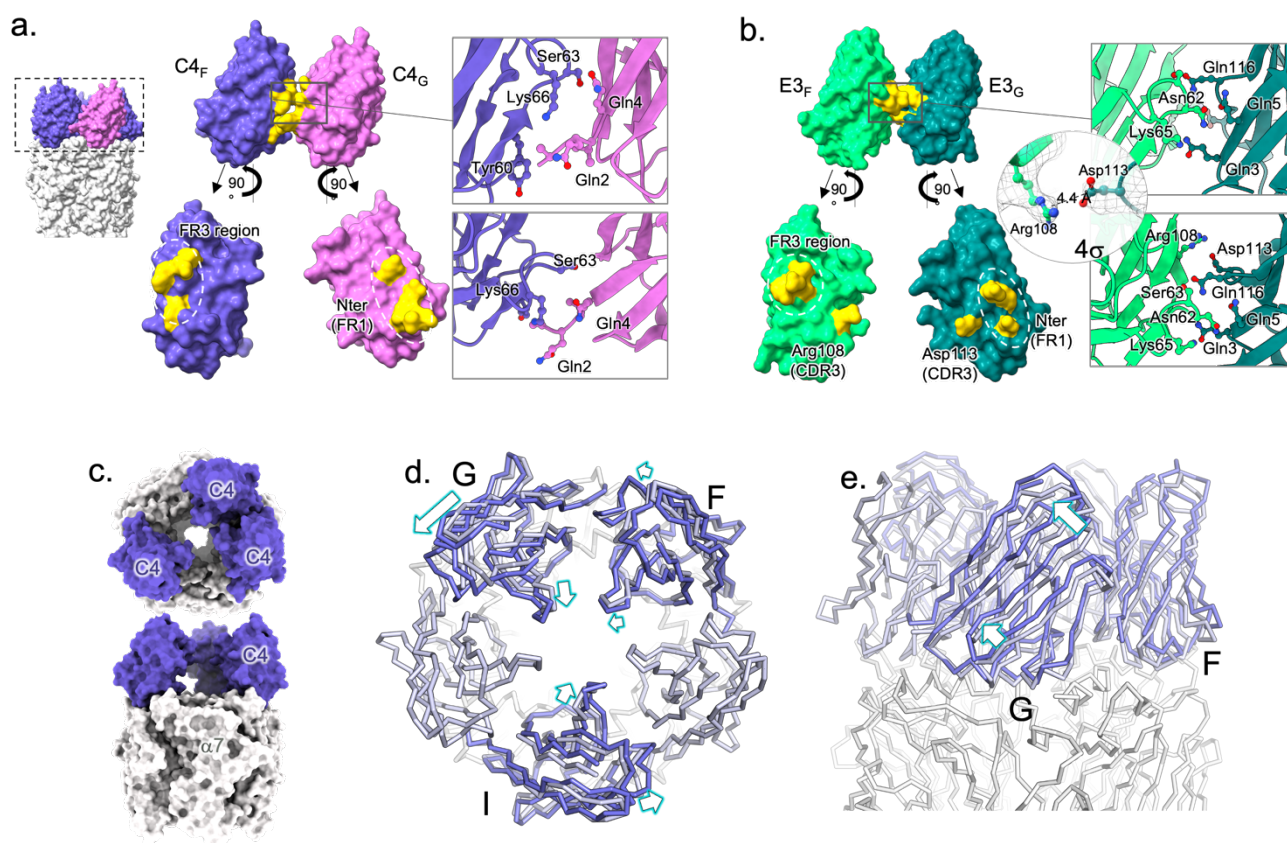


**Figure 5: Nanobody-nanobody interactions.**

- Surface representation of two adjacent C4 (F in purple, G in pink) in C4-Apo and their exploded view below. Residues at the interface are colored in yellow and their details are shown in cartoons and sticks in a close-up view (right).
- Surface representation of two adjacent E3 (F in light green, G in dark pink) in E3-Apo and their exploded view below. Residues at the interface are colored in yellow and their details are shown in cartoons and sticks in a close-up view (right). Additionally, the putative salt bond between Arg108 and Asp113 is detailed in a separate close-up view, with the density contoured at 4σ.
- Overview of the C4<sub>partial</sub>-Apo structure from the top (top) and the side (bottom) with α7 in grey and the three C4 molecules in purple.
- Superimposition of the C4<sub>partial</sub>-Apo on the C4-Apo structures, aligned on α7 ECD. Both structures are represented in ribbon, α7 in grey, C4 from C4<sub>partial</sub>-Apo in purple and C4 from C4-Apo in grey blue. Motion from C4-Apo to C4<sub>partial</sub>-Apo are highlighted with arrows. On the left, structures are seen from the top and show a lateral inclination of the nanobodies toward the anticlockwise subunit accompanied by a radial inclination towards the vestibule. On the right, structures are seen for the side, with the most displaced nanobody in front (chain G).

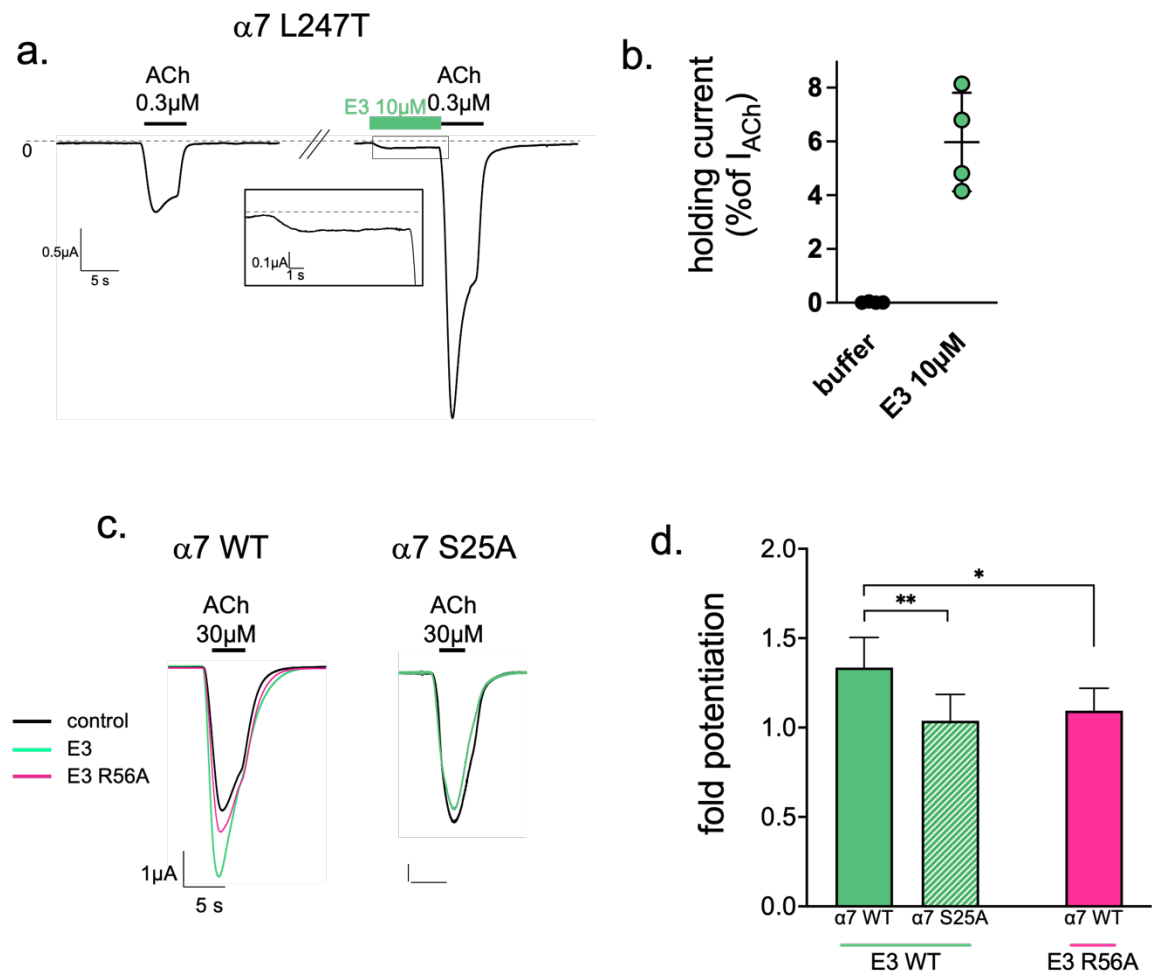


**Figure 6: Electrophysiological analysis of the potentiation by E3.**

- E3 direct activation on  $\alpha 7$  L247T mutant recorded by TEVC on *Xenopus* oocytes. Representative trace showing a first 0.3  $\mu$ M ACh application yielding slow-desensitizing currents. After 2-min washing, 10  $\mu$ M E3 was applied for 10 sec, evoking significant current, before 0.3  $\mu$ M ACh. A close-up view of the recording during E3 application is shown in a black box.
- Holding currents measured on  $\alpha 7$  L247T with or without 10  $\mu$ M E3 normalized with the non-potentiated response to 0.3  $\mu$ M ACh.
- Potentiation assays of E3-WT and E3-R56A on  $\alpha 7$  WT and of E3-WT on  $\alpha 7$ -S25A. Responses to 30  $\mu$ M ACh in the absence of E3 (black) are superimposed with response after 30 sec application of 1  $\mu$ M of E3 wild-type (green), or R56A (pink).
- Fold potentiation calculated on  $n \geq 4$  cells by E3-WT on  $\alpha 7$  WT and S25A mutant and of E3-R56A on  $\alpha 7$ -WT. Values were submitted to a unpaired t-test with \*  $p \leq 0.05$ , \*\*  $p \leq 0.01$

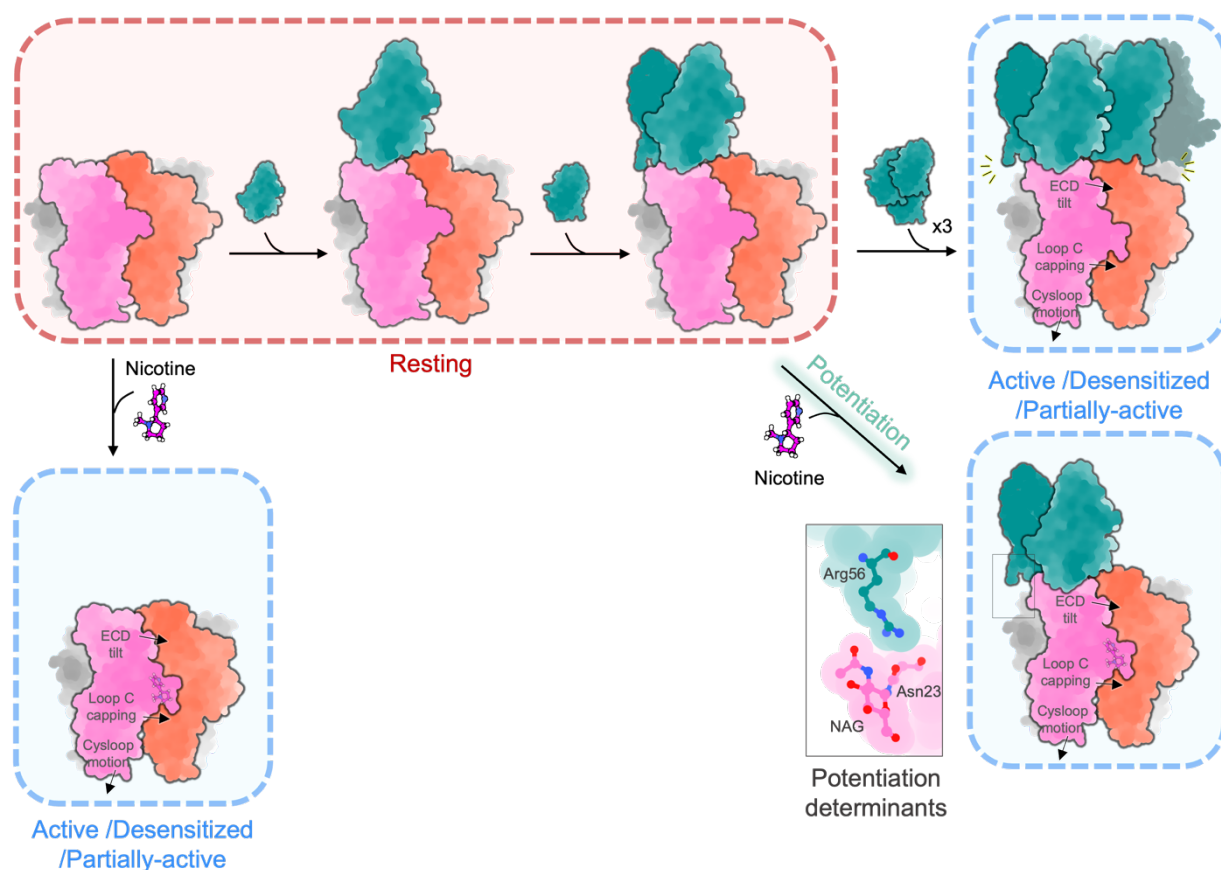
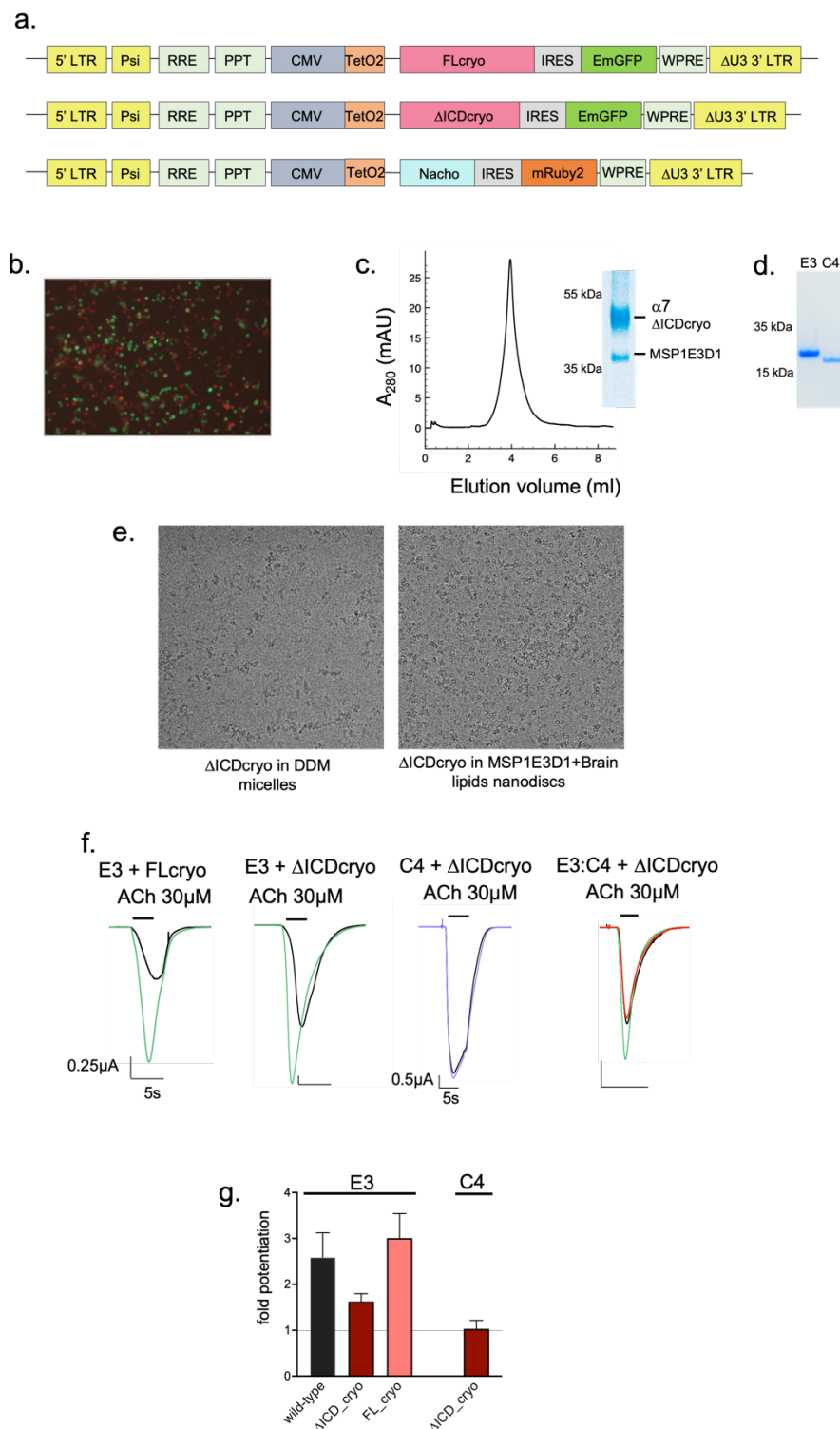


**Figure 7 : Hypothetical model for the allosteric mechanism mediating the PAM/agonist activity of E3.**

Cartoon representation of E3 (green) in complex with the  $\alpha 7$  ECD (with two subunits colored pink and orange). Nicotine alone is shown to elicit the transition for the resting to the active/desensitized conformation. This transition involves ECD tilt, loop C capping and cys-loop outward motion. Our data suggest that, in typical TEVC conditions with an E3 concentration below  $1 \mu\text{M}$ , potentiation of ACh-elicited response is caused by partial occupancy of the E3 binding sites, as arbitrarily illustrated here by the binding of two nanobodies. Interaction between Arg56 of E3 and a N-linked sugar of  $\alpha 7$  nearby the  $\alpha 7$ - $\alpha 7$  interface is critical for this potentiation. Cryo-EM data further show that higher concentrations ( $50 \mu\text{M}$ ) of E3 are required to saturate the receptor, a condition in which E3 triggers the activation/desensitization conformational change in the absence of nicotine.

## Figures supp



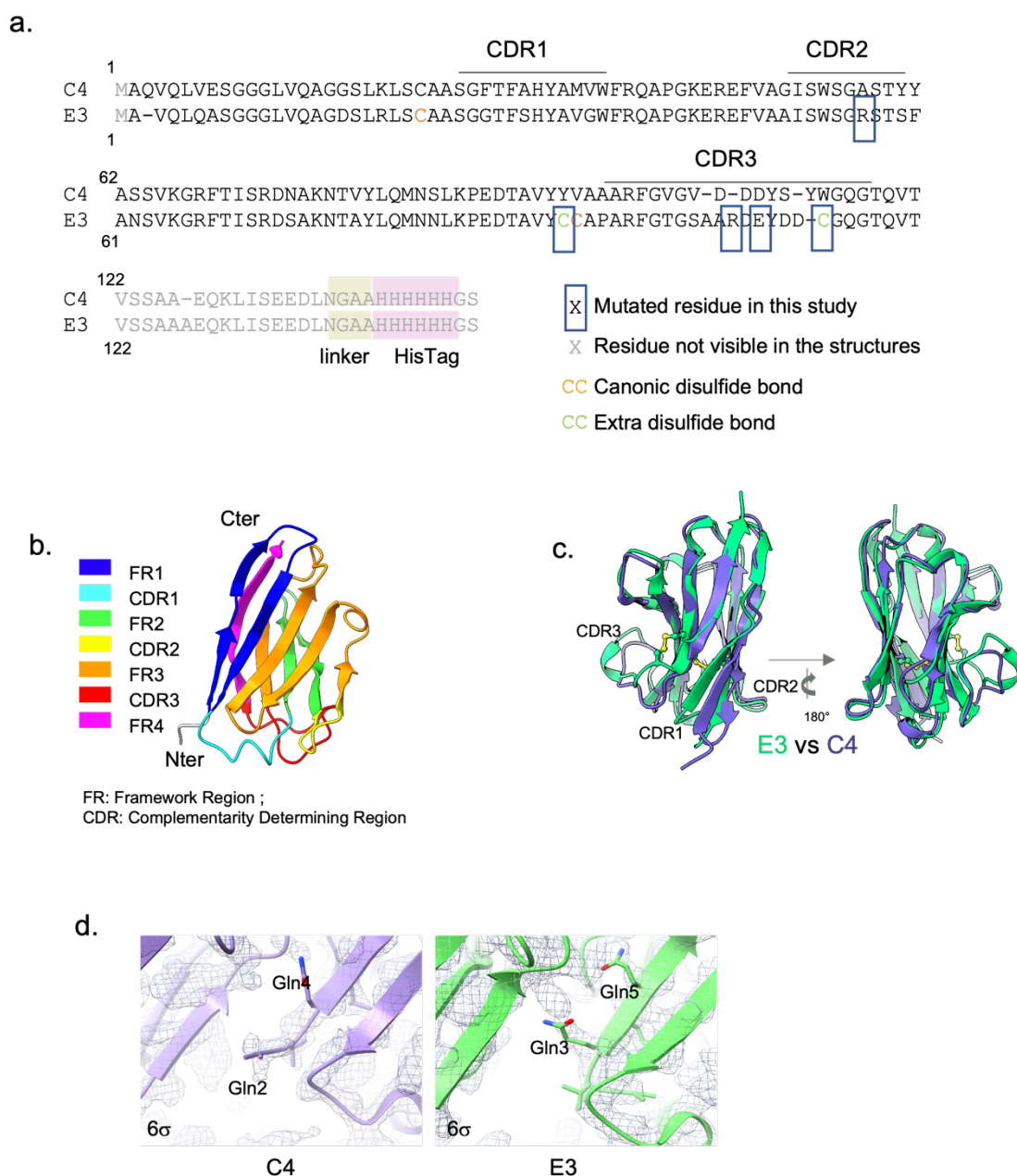
**Supplementary figure 1: Production of the  $\alpha 7$  nAChR and functional characterization of E3 WT and mutants**

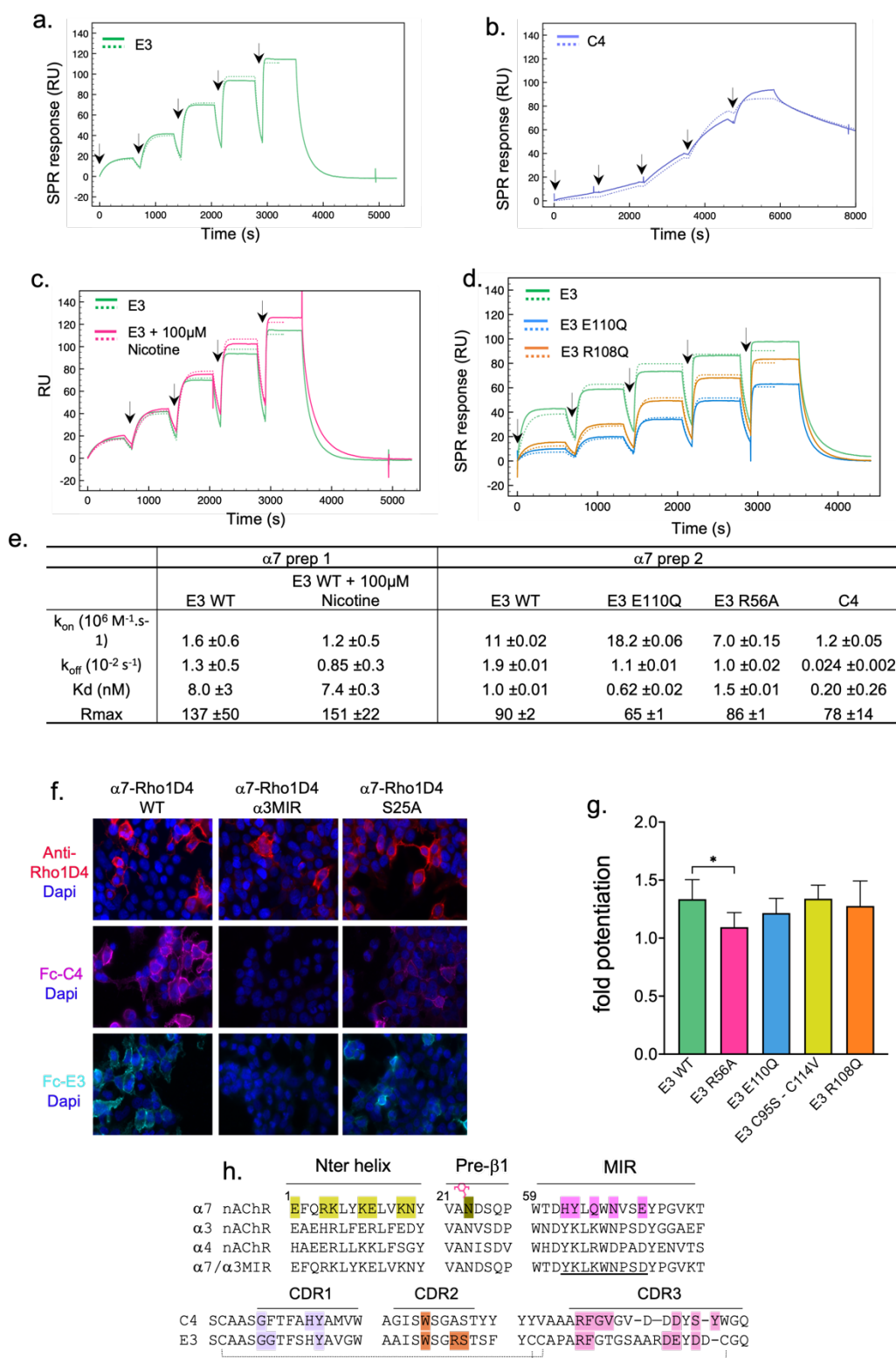
- a. Lentiviral transfer regions used in the study. LTR: Long Terminal Repeat sequence,  $\Delta$ U3: Deletion in 3'LTR rendering the virus "self-inactivating" (SIN) after integration, Psi: Packaging signal sequence; RRE: Rev Response Element cPPT: Central Polypurine Tract; CMV: Cytomegalovirus Promoter; TetO2: Tetracycline-controlled transcriptional activation

sequence ; IRES : Internal ribosome entry site of the encephalomyocarditis virus;  
WPRE: Woodchuck Hepatitis Virus Post-transcriptional Regulatory Element

- b. After transduction and induction, most cells exhibit orange and green fluorescence indicating efficient cell infection.
- c. Size-exclusion profile of  $\alpha 7\Delta$ ICDcryo reconstituted in nanodiscs and SDS PAGE of the concentrated sample before plunge freezing.
- d. SDS-PAGE of E3 and C4 after purification.
- e. Representative micrographs of  $\alpha 7\Delta$ ICDcryo in detergent micelles or reconstituted in nanodiscs, showing the presence of aggregates in the former.
- f. Representative TEVC recordings showing the potentiation of 30 $\mu$ M ACh-elicited currents upon a 30s pre-application of 1 $\mu$ M of E3 (green) or C4 (purple) or by 0.25 $\mu$ M E3 and 0.5 $\mu$ M C4 (red) with the indicated  $\alpha 7$  constructs.
- g. Fold potentiation of 30 $\mu$ M ACh currents determined with a 30sec pre-application of 1 $\mu$ M nanobody for the indicated constructs. Data are mean  $\pm$ sd for  $n \geq 4$ .



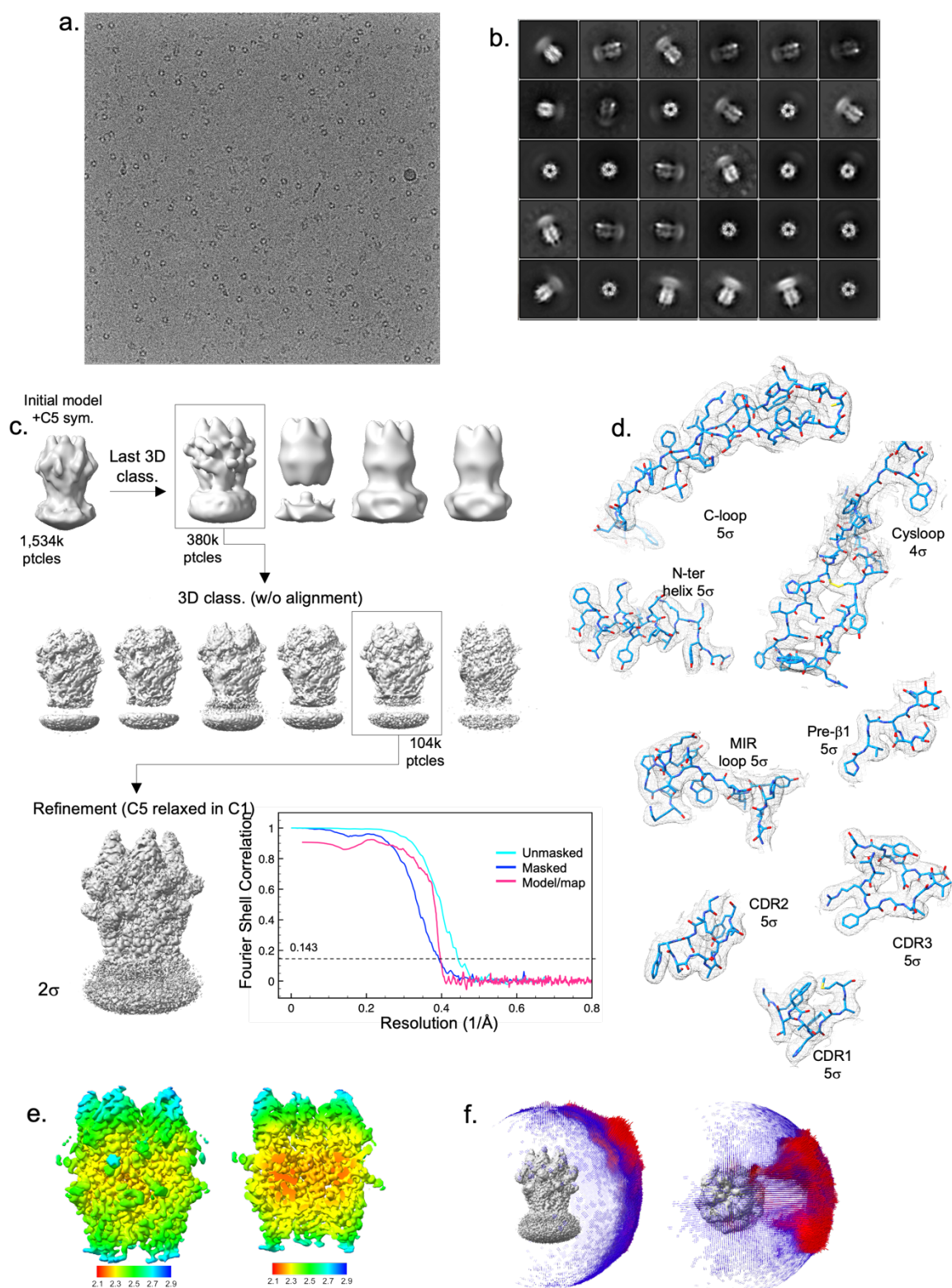




**Supplementary figure 4: characterization of the  $\alpha 7$  nAChR, C4, E3 and their mutants by SPR, immunofluorescence and electrophysiology**

- Real-time SPR monitoring of injections of increasing concentrations of E3 (black arrows) on purified  $\alpha 7\Delta$ ICDcryo reconstituted in nanodiscs. The dashed line shows the fitting curve used to determine the kinetic constants.
- Same as in a. with C4.

- c. Same as in a. with E3 (green) and E3 with 100 $\mu$ M nicotine in the running buffer (pink).
- d. Same as in a with E3 (green), E3 E110Q (blue) and E3 R108Q (orange).
- e. Kinetic and affinity constants determined by single cycle kinetics surface plasma resonance. E3 WT was first assayed with or without 100 $\mu$ M nicotine on a single  $\alpha$ 7 $\Delta$ ICDcryo nanodiscs preparation. Another preparation was used to perform the assay with E3 WT and its mutants and with C4. Data are mean  $\pm$ sd of 3 independent channels on the sensorchip.
- f. Immunofluorescence of C4 and E3 fused to Fc on HEK cells expressing  $\alpha$ 7 WT, S25A or the  $\alpha$ 7/ $\alpha$ 3MIR chimera. Top:  $\alpha$ 7 receptors are labelled using the Cter Rho1D4 tag (red), nuclei using Dapi (blue). Middle: Fc-C4 labelling is shown in purple, nuclei are labelled using Dapi (blue). Bottom: Fc-E3 labelling is shown in green, nuclei are labelled using Dapi (blue).
- g. Fold potentiation calculated by TEVC on  $n \geq 4$  cells by E3-WT and its mutants on  $\alpha$ 7-WT. Values were submitted to a paired t-test that is denoted with \*  $p \leq 0.05$  when a significant difference was found.
- h. Sequence alignments of the loops involved in binding. Top: alignment of the Nter helix, pre- $\beta$ 1 and MIR of  $\alpha$ 7,  $\alpha$ 3,  $\alpha$ 4 and the chimeric  $\alpha$ 7/ $\alpha$ 3MIR construct (with the chimeric sequence underlined). Key residues involved in binding are highlighted and the glycan on Asn23 depicted as a pink sugar. Sequence numbering is the one of  $\alpha$ 7. Bottom: alignments of the three CDR regions of C4 and E3. Key residues involved in binding are highlighted. Disulfide bonds of E3 are depicted by links between the two cysteines. CDR3s alignment is based on their local structure.

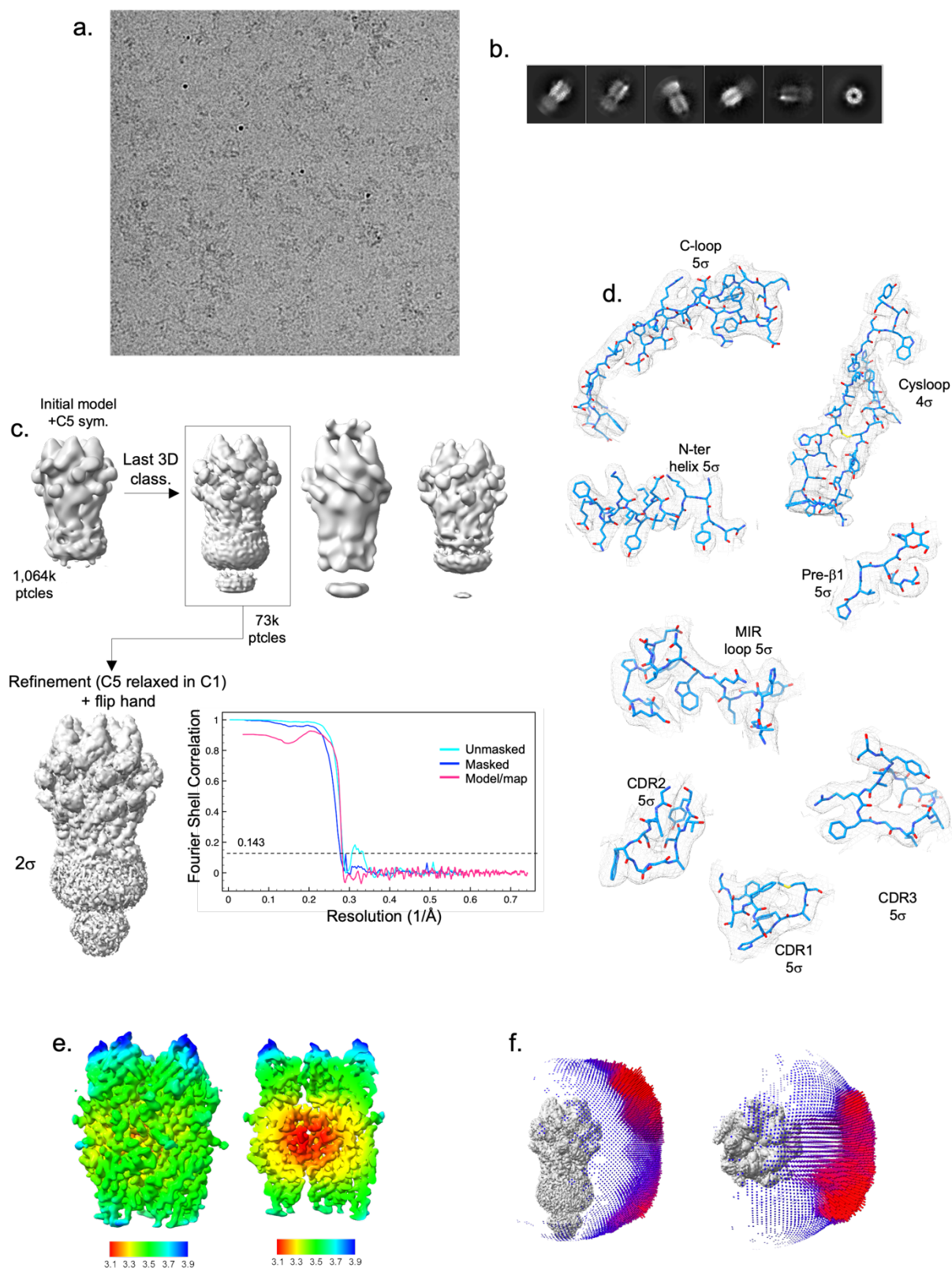


**Supplementary figure 5: Electron microscopy and 3D reconstruction of the C4-Apo data set**

- Representative micrograph of the C4-Apo dataset.
- Selected 2D class averages
- Flowchart of the 3D volume processing. A C5-symmetry was applied on the initial model for 3D classification with particles alignment. The best class particles were submitted to another 3D

classification round without alignment and high-resolution reaching particles further refined with a C5 symmetry relaxed in C1 (Relion 3D refine). Resulting volume is shown at  $2\sigma$  contouring with the FSC curves on its right.

- d. Representative densities and model building for the loop C, cys-loop, Nter helix, pre- $\beta$ 1, MIR of  $\alpha$ 7 and the three CDRs of C4 with the indicated contouring level
- e. Local resolution map calculated with Relion. The volume is shown at high contouring from the side and sliced in the vestibule.
- f. Angular distribution of the particles seen on the side and top views of the unsharpened map

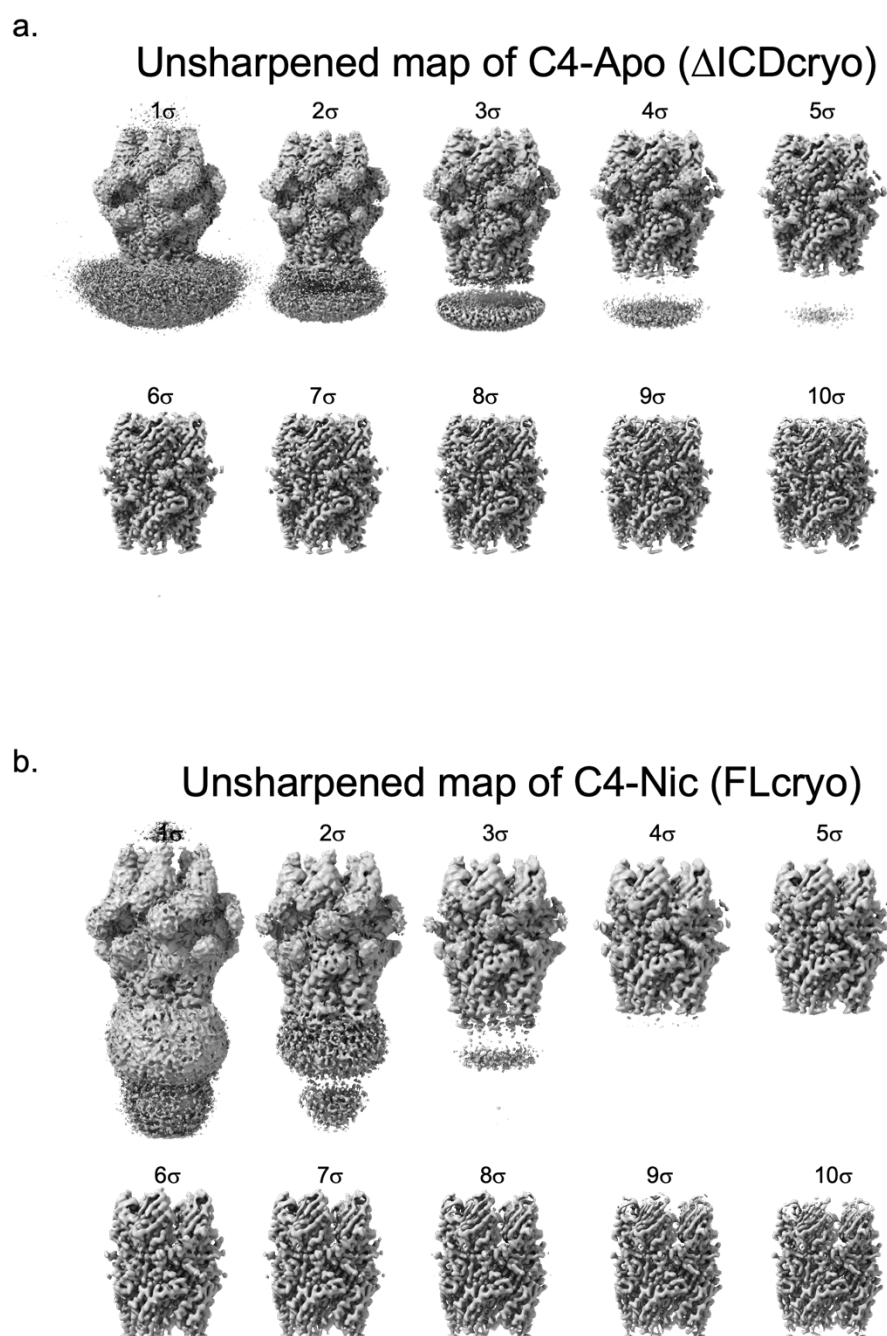


**Supplementary figure 6: Electron microscopy and 3D reconstruction of the C4-Nic data set**

- Representative micrograph of the C4-Nic dataset.
- Selected 2D class averages
- Flowchart of the 3D volume processing. A C5-symmetry was applied on the initial model for 3D classification with particles alignment. The best class particles were further refined with a C5

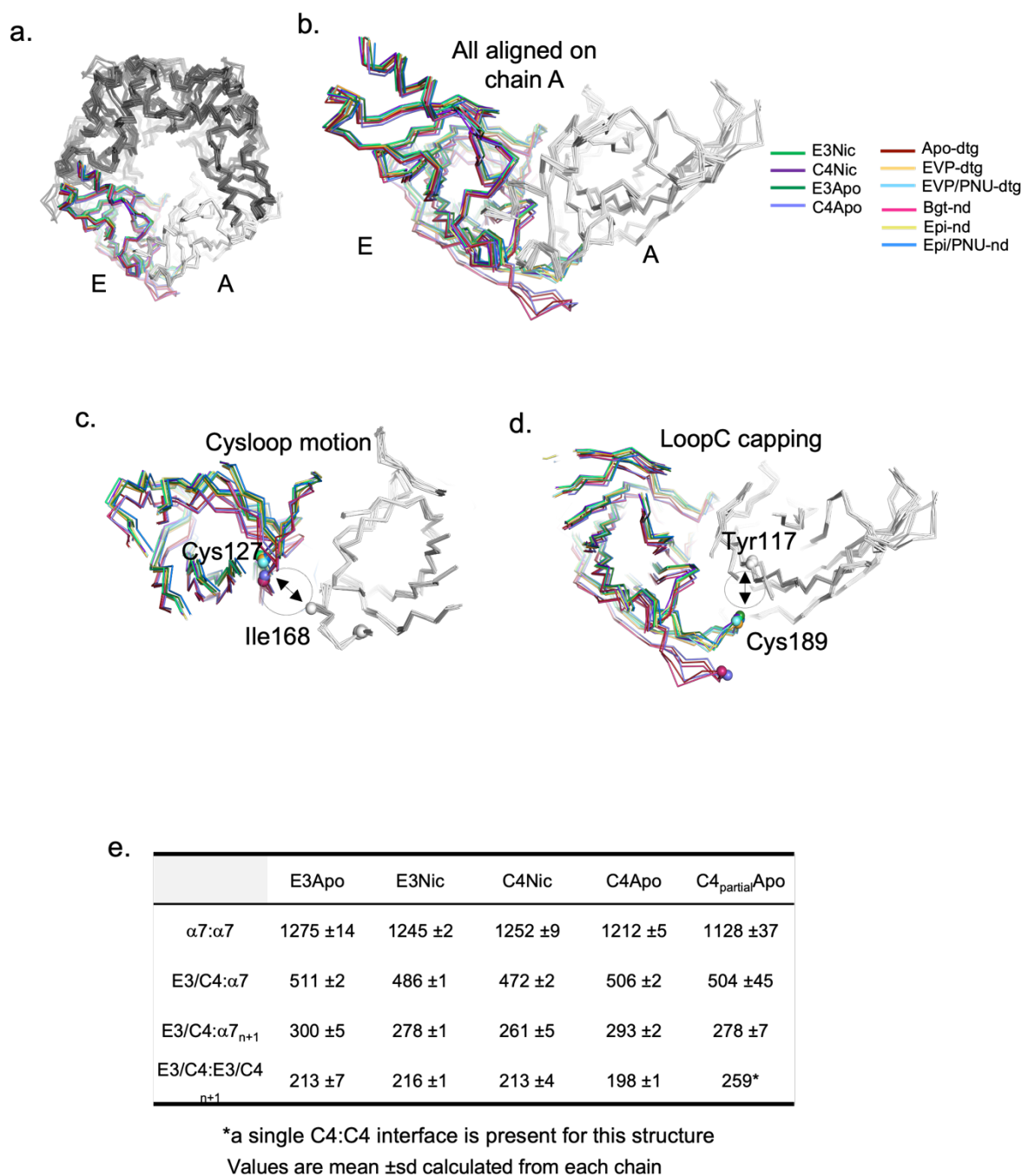
symmetry relaxed in C1 (Relion 3D refine). Resulting volume is shown at  $2\sigma$  contouring with the FSC curves on its right.

- d. Representative densities and model building for the loop C, cys-loop, Nter helix, pre- $\beta$ 1, MIR loop of  $\alpha$ 7 and the three CDR of C4 with the indicated contouring level
- e. Local resolution map calculated with Relion. The volume is shown at high contouring from the side and sliced in the vestibule.
- f. Angular distribution of the particles seen on the side and top views of the unsharpened map



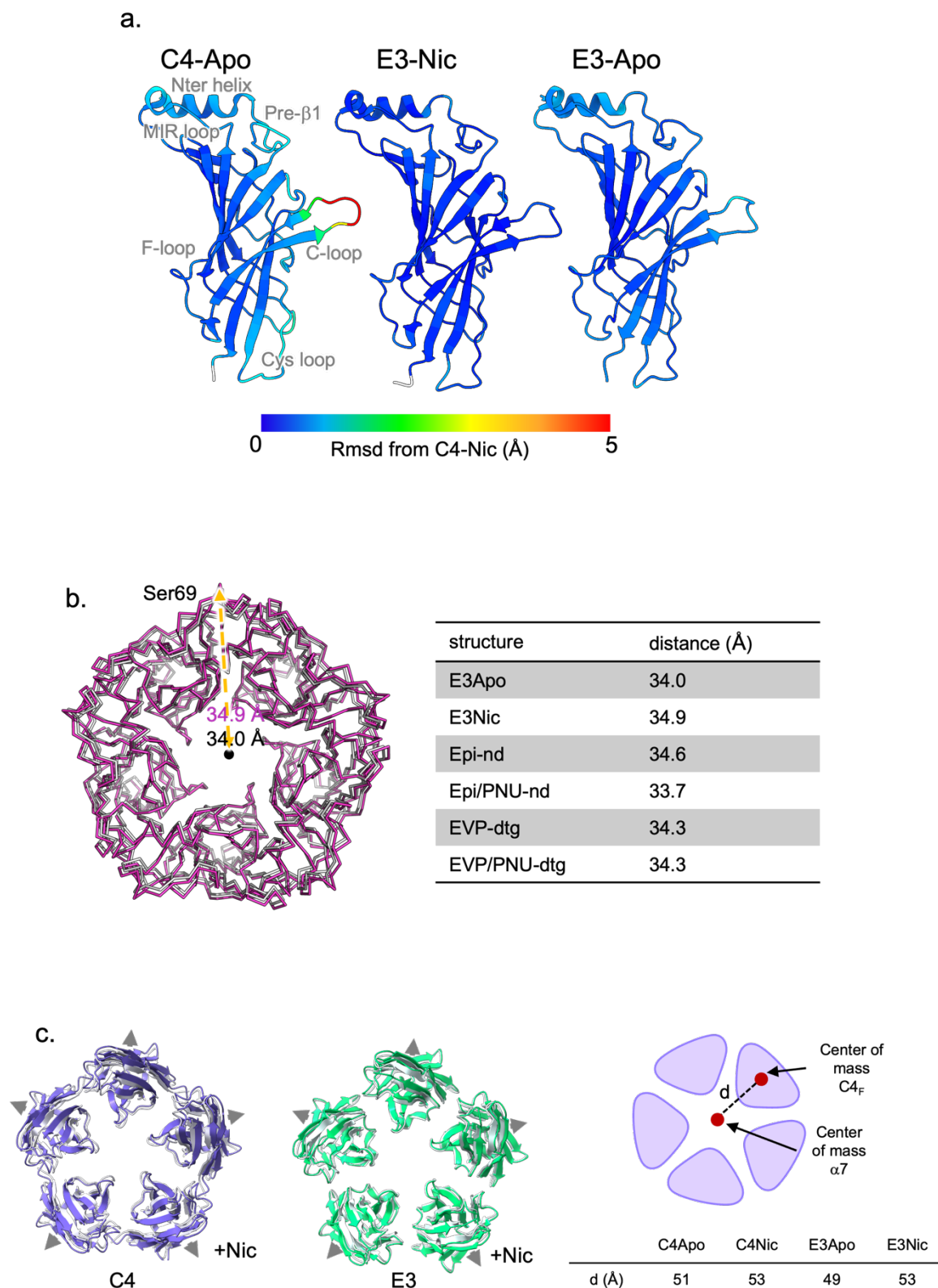
**Supplementary figure 7: Unsharpened cryo-EM maps of C4-Apo and C4-Nic**

- Various contouring levels applied to the C4-Apo density showing the flexibility of the transmembrane/nanodisc region that completely disappears at 6 $\sigma$ .
- Various contouring levels applied to the C4-Nic density showing the flexibility of the transmembrane/nanodisc and intracellular regions that completely disappear at 4 $\sigma$ .



### Supplementary figure 8: Analysis of the conformation of the $\alpha 7$ ECD in E3 and C4 co-structures

- $\alpha 7$  pentamers from known structures are aligned at the level of their chain A and represented as ribbons in top view.
- A dimer A-E of the aligned structures in a. is shown. Chains A are seen in grey and chains E according to the color-coding on the right.
- Same as in b. but clipped to reveal the cys-loop and its motion towards the chain A. The “cys-loop motion” distance measurement between the C $\alpha$  of Cys127 and Ile 168 is figured with an arrow.
- Same as in b. but clipped to reveal the Loop C and its motion towards the chain A. The “Loop C capping” distance measurement between the C $\alpha$  of Cys189 and Tyr117 is figured with an arrow.
- Interaction surface areas calculated using PISA (CCP4 suite) in  $\text{\AA}^2$ .

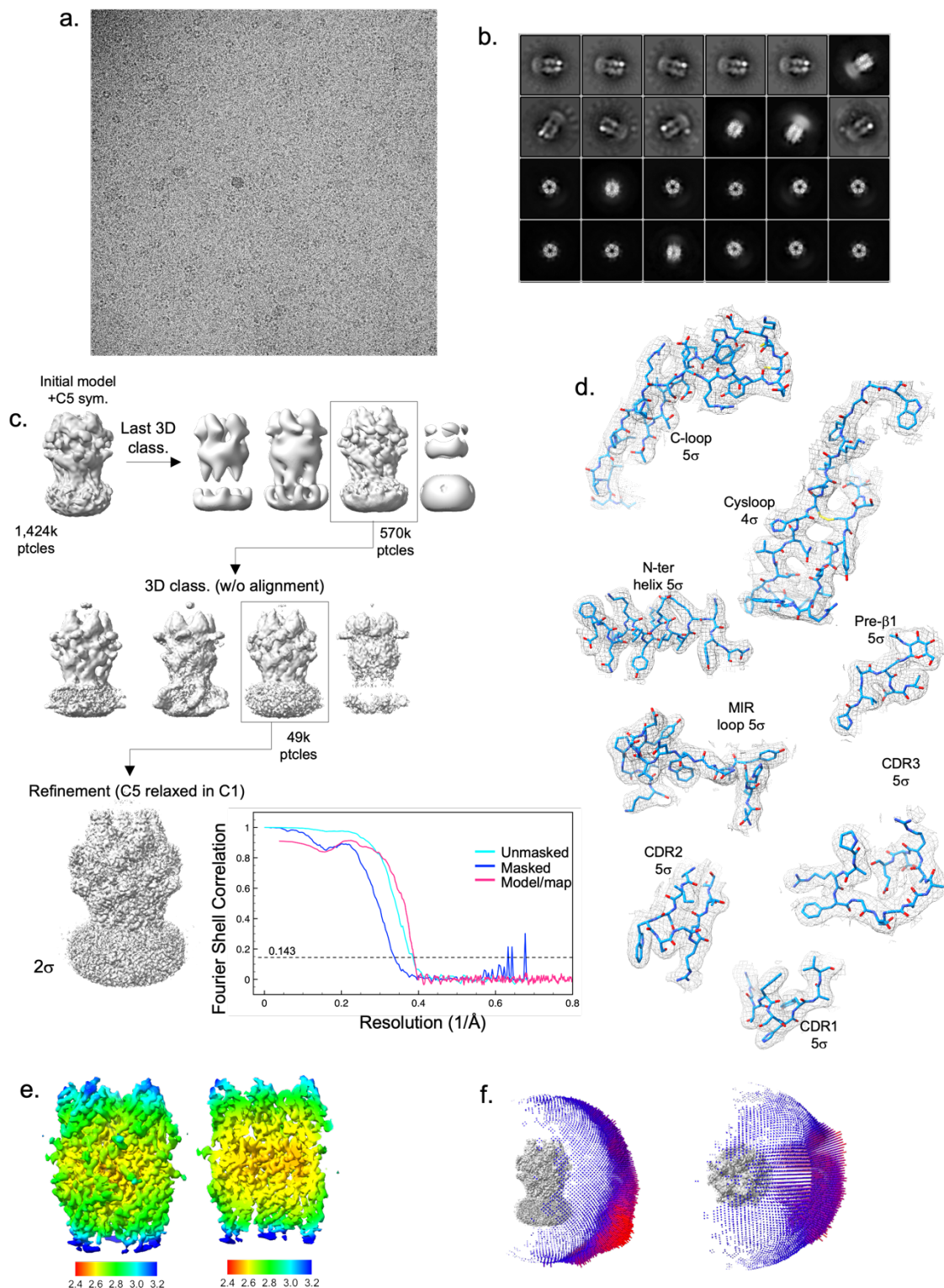


**Supplementary figure 9: Tertiary and quaternary reorganization of nanobody-bound structures in the presence of nicotine**

- a. Tertiary variations of  $\alpha 7$  between structures. C $\alpha$  rmsd were calculated in ChimeraX using the C4-Nic structure as reference upon superimposition of monomers. ECD monomer of C4-Apo, E3-Nic

and E3-Apo are shown in cartoons where  $C\alpha$  are colored according to the rmsd value, with the same range for all and shown in the color key.

- b. ECD expansion between E3-Apo and E3-Nic. Distances are measured between the  $C\alpha$  of Ser69 from chain A and the center of mass of the  $C\alpha$  of the five Ser69 which figure the middle of the upper part of the ECD. The distance is shown on a top view of the E3-Apo (grey) and E3-Nic (pink) aligned and represented in ribbons. The table shows the values of this distance on several structures. Note that the expansion is absent between the two detergent structures and is similar for the two pairs of nanodisc structures.
- c. Nanobodies expansion upon nicotine binding. With both nanobodies, we observed a small outward motion of the nanobodies molecules upon nicotine binding, as represented from the top with Apo structures in white and nicotine-bound structures in purple and green respectively. We found this motion to be around 2-3 Å by measuring the distance between the center of mass of one nanobody and the center of mass of  $\alpha 7$  (summarized in the table).

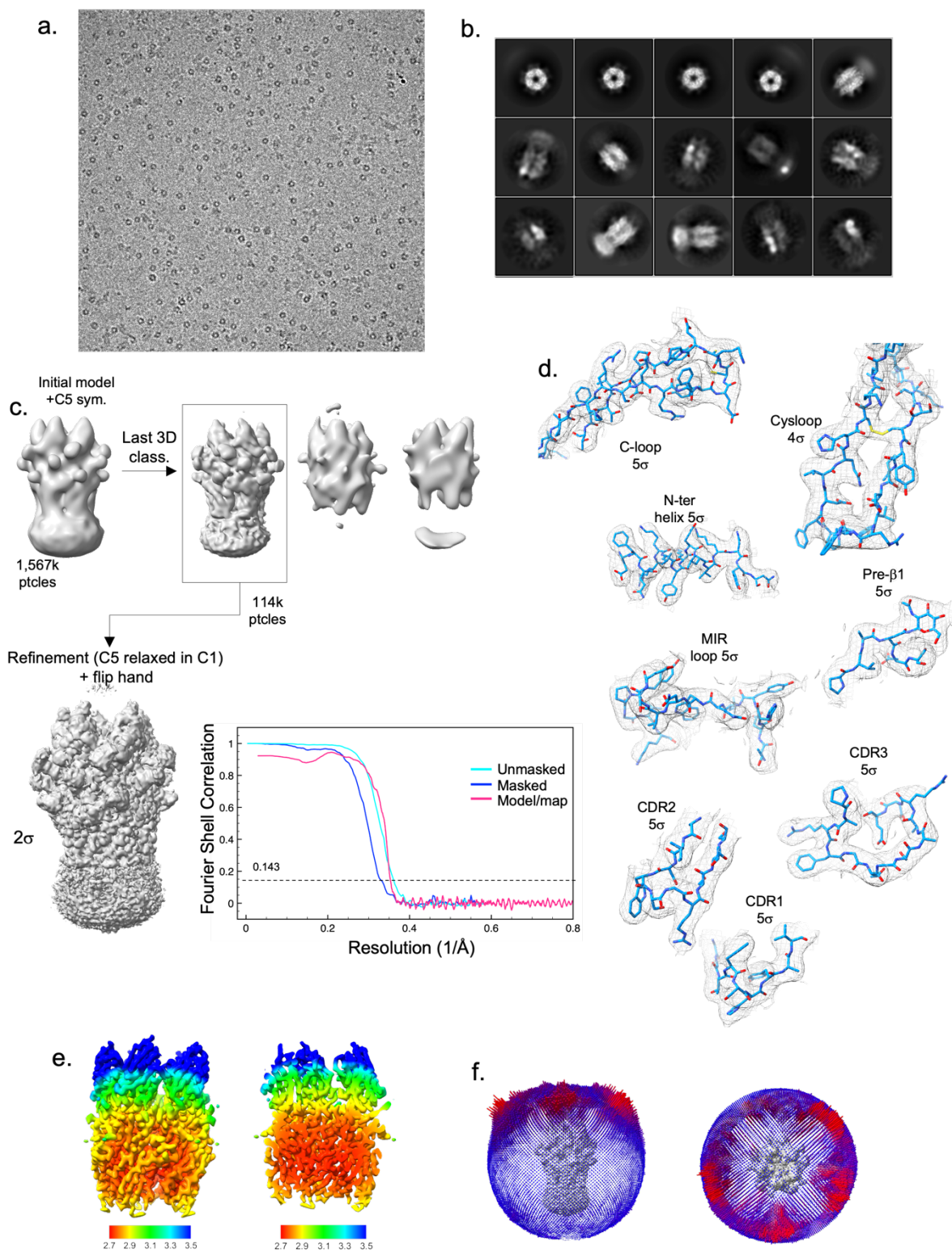


**Supplementary figure 10: Electron microscopy and 3D reconstruction of the E3-Apo data set**

- Representative micrograph of the E3-Apo dataset.
- Selected 2D class averages
- Flowchart of the 3D volume processing. A C5-symmetry was applied on the initial model for 3D classification with particles alignment. The best class particles were submitted to another 3D classification round without alignment and high-resolution reaching particles further refined with a

C5 symmetry relaxed in C1 (Relion 3D refine). Resulting volume is shown at  $2\sigma$  contouring with the FSC curves on its right.

- d. Representative densities and model building for the loop C, cys-loop, Nter helix, pre- $\beta$ 1, MIR of  $\alpha$ 7 and the three CDRs of E3 with the indicated contouring level.
- e. Local resolution map calculated with Relion. The volume is shown at high contouring from the side and sliced in the vestibule.
- f. Angular distribution of the particles seen on the side and top views of the unsharpened map.

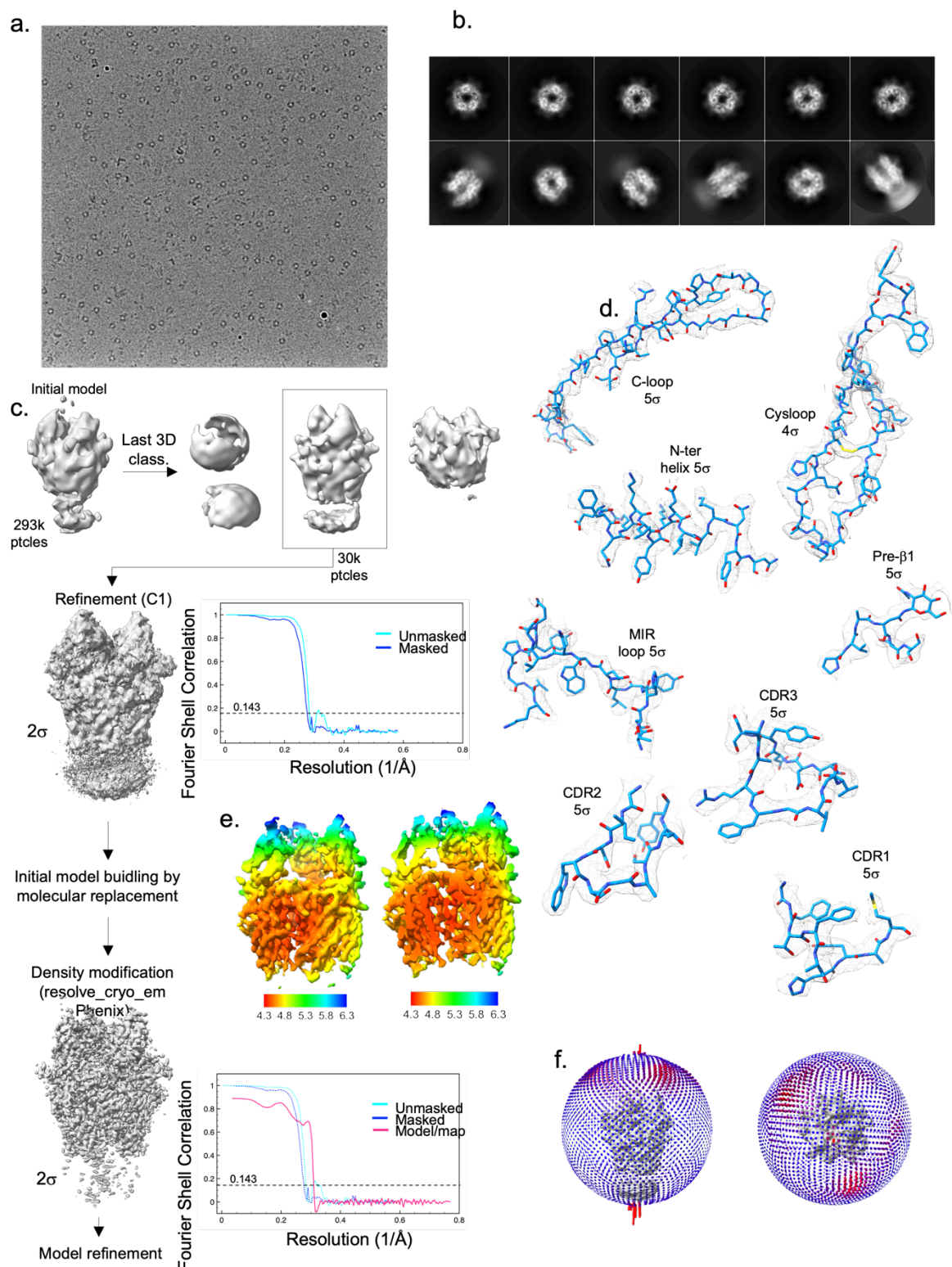


**Supplementary figure 11: Electron microscopy and 3D reconstruction of the E3-Nic data set**

- Representative micrograph of the E3-Nic dataset.
- Selected 2D class averages
- Flowchart of the 3D volume processing. A C5-symmetry was applied on the initial model for 3D classification with particles alignment. The best class particles were further refined with a C5

symmetry relaxed in C1 (Relion 3D refine). Resulting volume is shown at  $2\sigma$  contouring with the FSC curves on its right.

- d. Representative densities and model building for the loop C, cys-loop, Nter helix, pre- $\beta$ 1, MIR of  $\alpha$ 7 and the three CDRs of E3 with the indicated contouring level.
- e. Local resolution map calculated with Relion. The volume is shown at high contouring from the side and sliced in the vestibule.
- f. Angular distribution of the particles seen on the side and top views of the unsharpened map.

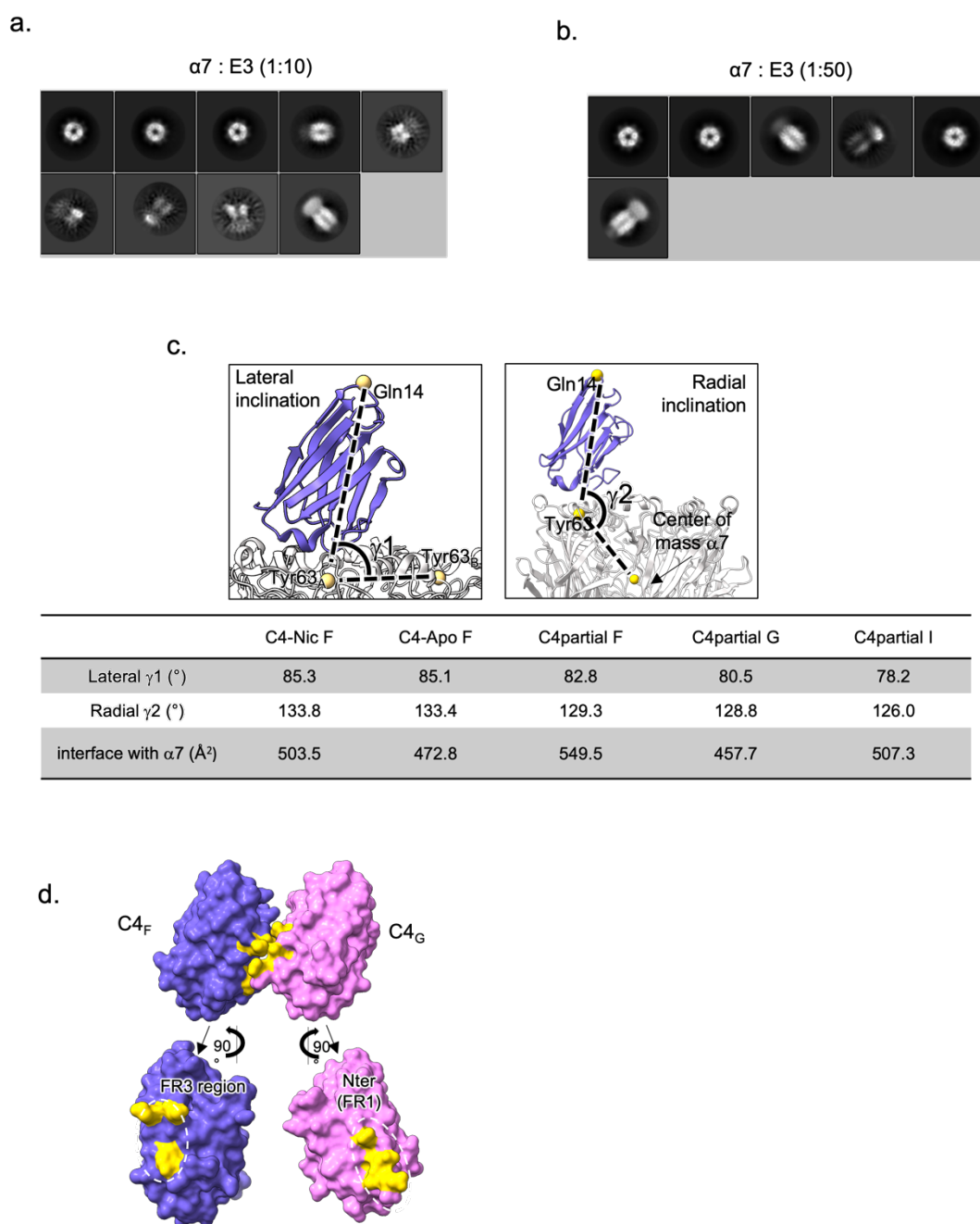


**Supplementary figure 12: Electron microscopy and 3D reconstruction of the C4partial-Apo data set**

- Representative micrograph of the C4partial-Apo dataset
- Selected 2D class averages
- Flowchart of the 3D volume processing. No symmetry was applied on the initial model for 3D classification with particles alignment. The best class particles were further refined (Relion 3D refine). Resulting volume is shown at 2σ contouring with the FSC curves on its right. After a first

model building, the density and the model were subjected to density modification in Phenix, resulting in a volume allowing the refinement of a protein model at 3.4 resolution shown at  $2\sigma$  contouring with the FSC curves on its right

- d. Representative densities and model building for the loop C, cys-loop, Nter helix, pre- $\beta$ 1, MIR of  $\alpha$ 7 and the three CDRs of C4 with the indicated contouring level.
- e. Local resolution map calculated with Relion. The volume is shown at high contouring from the side and sliced in the vestibule.
- f. Angular distribution of the particles seen on the side and top views of the unsharpened map.



### Supplementary figure 13: Analysis of the C4partial-Apo dataset

- Preliminary work was done with lower concentration of E3 in the grids (10 $\mu$ M) and early 2D classes showed heterogeneity with most classes showing 4 molecules bound to  $\alpha 7$ .
- Grids prepared the same day with 50 $\mu$ M E3 showed a vast majority of particles with 5 E3 molecules bound.
- Orientation of the C4 molecules in the C4partial-Apo structure. The lateral inclination angle is defined between the C $\alpha$  of Gln14 in C4, of Tyr63 in the  $\alpha 7$  chain below and of Tyr63 of the complementary  $\alpha 7$  subunit. The radial inclination angle is defined between the C $\alpha$  of Gln14 on C4, of Tyr63 on the  $\alpha 7$  subunit below and the center of mass of the  $\alpha 7$  pentamer.
- Surface representation of the two adjacent C4 (F in purple, G in pink) in the C4partial-Apo dataset and their exploded view below. Residues at the interface are colored in yellow.

	C4-Apo (EMDB-) (PDB )	C4-Nic (EMDB-(PDB	E3-Apo (EMDB) (PDB )	E3-Nic (EMDB) (PDB )	C4partial-Apo (EMDB) (PDB )
<b>Data collection and processing</b>					
Microscope	IC-Krios1 EMBL, Heidelberg	Titan-Krios IP, Paris	IC-Krios1 EMBL, Heidelberg	Titan-Krios IP, Paris	Glacios IP, Paris
Magnification	165 000	105 000	165 000	105 000	150 000
Voltage (kV)	300	300	300	300	200
Electron exposure (e-/Å <sup>2</sup> )	40	40	40	40	50
Defocus range (µm)	-0.6 to -1.6	-0.6 to -2.2	-0.6 to -1.6	-0.6 to -2.2	-0.8 to -2.4
Pixel size (Å)	0.731	0.86	0.731	0.86	0.96
Symmetry imposed	C5	C5	C5	C5	C1
Movies	20151	5103	11090	5757	4506
Initial particle images (no.)	1534810	1064223	1424083	1566807	293673
Final particle images (no.)	104409	73690	49462	114385	29644
Map resolution (Å)	2.3	3.4	2.7	2.8	4.4
FSC threshold	0.143	0.143	0.143	0.143	0.143
Map resolution range (Å)	2.15-8.43	3.08-4.22	2.5-11.1	2.71-7.79	4.38-12
<b>Refinement</b>					
Initial model used (PDB code)					
Model resolution (Å)	2.46	3.51	2.53	2.7	3.4
FSC threshold	0.143	0.143	0.143	0.143	0.143
Map sharpening <i>B</i> factor (Å <sup>2</sup> )	-100	-100	-100	-100	-100
Model composition					
Non-hydrogen atoms	13465	13615	13010	13655	11145
Protein residues	1635	1635	1645	1660	1393
Ligands	NAG: 20	NCT:5 NAG: 20	NAG: 20	NCT: 5 NAG: 20	NAG: 20
<i>B</i> factors (Å <sup>2</sup> )					
Protein	72.0	78.1	38.64	84.9	29.2
Ligand	85.4	78.5	64.14	100.0	54.4
R.m.s. deviations					
Bond lengths (Å)	0.005	0.003	0.003	0.003	0.003
Bond angles (°)	0.812	0.506	0.597	0.480	0.643
Validation					
MolProbity score	2.36	2.33	2.33	1.94	2.02
Clashscore	11.86	20.95	10.19	11.27	6.51
Poor rotamers (%)	4.17	3.64	3.35	1.40	0.18
Ramachandran plot					
Favored (%)	95.67	91.15	93.91	96.16	85.04
Allowed (%)	4.33	8.85	5.97	3.84	13.36
Disallowed (%)	0	0	0.12	0	1.60

**Supplementary Table 1 Cryo-EM data collection, refinement and validation statistics**

		R-like states			A/D-like states						
		C4Apo	Apo- (7EKI)	Bungaro (7KOO)	E3Apo	E3Nic	C4Nic	EVP (7EKP)	EVP+PNU (7EKT)	Epib+PNU (7KOX)	Epib (7KOQ)
R-like states	C4Apo		0.805	<b>0.595</b>	0.73	1.16	1.27	0.974	1.02	1.13	1.34
	Apo- (7EKI)			0.5	1.27	0.96	1	0.95	1.01	1.53	1.27
	Bungaro (7KOO)				1.18	1.11	1.22	1.04	1.09	1.42	1.29
A/D-like states	E3Apo					0.836	0.9	0.62	0.67	<b>0.454</b>	0.86
	E3Nic						0.29	0.62	0.54	1.03	<b>0.51</b>
	C4Nic							0.64	0.59	1.07	<b>0.56</b>
	EVP (7EKP)								0.23	0.83	0.64
	EVP+PNU (7EKT)									0.81	0.55
	Epib+PNU (7KOX)										0.85

	Structures in detergent micelles
	Structures in saposin/azolectin nanodiscs
	Best match

**Supplementary Table 2 : C $\alpha$  rmsd values calculated on the pentamer of ECD for the indicated structures**

			CDR1			CDR2	CDR3										
			Gly27	His32	Tyr33	Trp54	Arg101		Phe102		Gly103	Val104	Asp109			Ser111	Tyr112
			CO	NHε	OHη	NHε	CO	NHη	Bz	CO	N	Cγ	OHδ	N	CO	OHγ	OHη
Nter helix n+1	Glu1	N				+											
	Arg4	NHη							+	+							
	Lys5	Cγ									+						
		NHε															
	Lys8	NHε															
Nter helix	Glu9	OHδ			+										+	+	
		CO															
	Lys12	N									+			+			
		NHε															
	Asn13	NHδ					+		+				+	+			
		OHδ										+	+				
Pre-β1	Asn23-NAG	COOH															
	Asn23	CO															
MIR	His62	NHε															
	Tyr63	CO						+									
		Bz							+								
	Gln65	CO						+									
		OHε		+													
	Glu70	CO															
		OHε	+														

### Supplementary Table 3: Atomic contacts between C4 and $\alpha$ 7.

Contacts were selected when the inter-atomic distance is below 4 Å , unless specified

			CDR1			CDR2			CDR3						
			Gly26	Gly27	Tyr32	Trp53	Arg56	Ser57	Arg100		Phe101		Asp109	Glu110	Asp112
			CO	N	OH $\eta$	Indol	NH $\eta$	OH $\gamma$	CO	NH $\eta$	Bz	CO	OH $\delta$	CO	OH $\delta$
Nter helix n+1	Glu1	N													
	Arg4	NH $\eta$								+		+			
	Lys5	C $\gamma$													
		NH $\epsilon$					+								
	Lys8	NH $\epsilon$											+	+	*
Nter helix	Glu9	OH $\delta$			+						+				
		CO								+					
	Lys12	N													
		NH $\epsilon$													+
	Asn13	NH $\delta$									+				+
		OH $\delta$													
Pre- $\beta$ 1	Asn23- NAG	COOH					+								
	Asn23	CO					+								
MIR	His62	NH $\epsilon$				+									
	Tyr63	CO													
		Bz									+	+			
	Gln65	CO								+					
		OH $\epsilon$													
	Glu70	CO	+	+											
		OH $\epsilon$													

**Supplementary Table 4: Atomic contacts between E3 and  $\alpha$ 7.**

Contacts were selected when the inter-atomic distance is below 4 Å, unless specified

\* 4.4 Å